POLITECNICO DI TORINO

Master Degree Course in

Biomedical Engineering

Master Degree Thesis

Automatic microtubule tracking in fluorescence images of cells doped with increasing concentrations of taxol and nocodazole

Supervisor

Prof. Gabriella OLMO

Candidate

Marilena VARRECCHIA

April 2018

Acknowledgements

Over these years, I have learned and grown up a lot, from both an academic and personal standpoint. In these few lines I would like to thank the people who have mostly contributed to this growth and made this work possible.

Foremost, I would like to thank my supervisor, Prof. Gabriella Olmo, for her guidance, great willingness, persistent support and patience demonstrated in the countless meetings over these months. I am extremely grateful for having had the opportunity to work with her at this project.

I would also like to thank Dr. Marta Gai, Prof. Marco Grangetto, Prof. Ferdinando di Cunto, and Joshua for their availability and the valuable discussions on the topic.

I wish to express my sincere gratitude to my whole family, especially to my parents for the support and wise advice, to my brother (and messy roommate) for having constantly endured my stress, and to my uncles and cousins for constantly having believed in me.

My gratitude also goes to all my fellows and friends that have been a part of this journey. In particular, thanks to: Francesca for all the dinners and great company, especially over these months, my *lifecoach* Giorgia for all her helpful hints, and, above all, for her patience; Ilaria, for good (and bad) times spent on our *wonderful* projects; Domenico, for having shared his food experiments; Michele, for all the laughter throughout our classes; and Francesca and Cristina for morally helping me in times of need.

And last but not least, I am grateful to Ester and Stefania, because no matter how far we are or how much time elapses, I can always rely on them.

Abstract

This work aims to design a tool to automatically analyze astral microtubule behavior in confocal images.

Microtubules are polymers involved in several cell functions; specifically, the astral ones (i.e. a microtubule specific category) are involved in mitotic spindle assembly during mitosis. Indeed, when the mitotic spindle is not correctly oriented, abnormal chromosome segregation can occur, and pathological conditions, related to specific gene mutations, can arise.

Nowadays, image processing is applied in a wide range of areas, such as remote sensing (e.g. video surveillance), human-machine interface, biology, medicine. Nevertheless, focusing on biological applications, it is worth pointing out that molecules make up complex and dynamic systems, generating a big amount of data. This is the reason why data post-processing and mathematical models of molecular structures are necessary in order to understand cell dynamics.

Over the years, a lot of software-based imaging techniques have been developed to support the biologists in their experiments. These approaches take into account the extreme problem complexity, that is related to both equipment (i.e. microscopy) and cell culture, and compromises the global image quality. The main issues are the limited instrument resolution and the different noise processes that are present in movies (e.g. photon shot noise, background noise, dark current, photobleaching).

Due to the scenario high variability, at present, a standard protocol does not exist for the analysis of such images; hence, biologists still manually review samples. It is clearly a huge, time-consuming and hardly reproducible task.

This is the reason why the project has been developed to provide a support to researchers.

Our algorithm evaluates microtubule *dynamic instability* (i.e. a characteristic polymer behavior) thanks to a *detection* and a *tracking* procedure, both based on traditional image processing techniques.

In order to assess the algorithm performance, nocodazole and taxol-doped cells have been taken into account, as they have known effects on cell cultures.

Moreover, given the lack of a *ground truth*, the feature extracted with our algorithm are compared to those of another algorithm, developed at University of Turin, and to some manually computed data; in both cases; the comparisons refer to the same dataset.

Finally, the work is compared with other approaches that can be found in literature, with good results.

It is worth pointing out that the proposed approach has been developed as standalone software and it is currently being used by biologists of Department of Molecular Biotechnology and Health Sciences of Turin.

List of acronyms

+TIP	Microtubule plus-end tracking protein
A-MT	Astral microtubule
EB-EGFP	Fluorescently-tagged End Binding Protein
ECM	Extracellular matrix
GFP	Green fluorescent protein
GTP	Guanosine-5'-triphosphate
GUI	Graphical user interface
IMM	Interacting Multiple Model
K-MT	Kinetochore microtubule
LPF	Low pass filter
MAP	Microtubule-associated protein
MCPH	Human primary microcephaly
MT	Microtubule
nK-MT	Non-kinetochore microtubule
PDA	Probabilistic data association
PMM	Piecewise-stationary motion model
PMMS	Piecewise-stationary motion model smoother
PSF	Point spread function
ROI	Region of interest
SEM	Standard error of the mean
SNR	Signal-to-noise ratio

Index of contents

Acknowledgements .... **i**

Abstract .... **ii**

List of acronyms .... **iv**

Introduction **1**

1.1 Microtubules 3

1.2 Microtubule structure 4

1.3 Microtubule function 6

1.4 Microtubule detection 7

1.4.1 Fluorescence 8

1.4.2 Confocal microscope 9

1.4.3 Fluorophores 10

Microtubules detection and tracking: state of the art **13**

2.1 Probabilistic approach 15

2.2 Deterministic approach 18

2.2.1 Combined approach 20

2.3 Approach based on machine learning 21

Dataset description 23

3.1 Cell culture 24
3.2 General information and parameters 24
3.3 Noise description 26
3.4 Statistical analysis 29
  3.4.1 Signal-to-noise ratio 29
3.5 Spectral analysis 31
  3.5.1 Two-dimensional Fourier Transform 31

Algorithm implementation 34

4.1 Algorithm calibration 34
4.2 Denoising 35
  4.2.1 Wiener filter 35
  4.2.2 LOG-Wiener Transform 37
4.3 Particle detection 40
  4.3.1 Comet detection threshold 40
  4.3.2 Local maxima searching 40
4.4 Microtubule plus-end tracking 42
  4.4.1 Partial tracks 42
  4.4.2 Final tracks reconstitution 45
4.5 Microtubule dynamic analysis 45
  4.5.1 Tracks screening 46
  4.5.2 Parameter calculation 47
4.6 Graphical user interface 49

Results 50

5.1 General remarks 51

5.2 Nocodazole results 52

5.3 Taxol results 56

5.4 Statistical data analysis 61

5.5 Feature correlation 62

5.6 Algorithm performance 63

  5.6.1 Comparison with *Algorithm 2* 63

  5.6.2 Comparison with *manual* 67

  5.6.3 Comparison with *Algorithm 3* and *Algorithm 4* 68

Conclusion and future directions 73

References 75

Chapter 1

Introduction

The detection and tracking of objects in digital images has become over the years an important application allowing to save time and to achieve reliability in the analysis process. Nowadays, image processing techniques are powerful tools applied in a wide range of areas, such as remote sensing (e.g. video surveillance), human-machine interface, biology, medicine.

In the biomedical field, image processing is employed for both diagnostic and therapeutic purposes, supporting physicians in their diagnosis and reducing issues related to intra and inter-subject variability.

This work is focused on the analysis of molecular biology images. In this area, image processing has led to significant progress in the early detection, monitoring, and diagnosis accuracy, thanks to the possibility of visualizing and measuring *in vivo* the cellular and molecular behaviors.

However, molecules make up complex and dynamic systems generating a big amount of data that require post-processing for their interpretation [1]. Moreover, to tackle this complicated issue, mathematical models of the molecular structures are necessary.

Over the years, many image processing tools have been developed to support the biologists in their research, but the limited resolution of microscopes and the high dynamicity of the particles of interest impact the software accuracy and precision.

Nowadays, fluorescence microscopy is the main imaging tool used to carry out *in vivo* studies of biologic processes in cells [1], allowing to follow the behaviors of single molecules. A major step forward in the light microscopy is related to the discovery of a naturally fluorescent protein in living organisms, the *GFP* (green fluorescent protein) [1]. Since then, other markers, with different spectral properties, have been engineered for labelling various types of proteins and cellular structures. This allows biologists to detect specific kinds of genes, to evaluate their kinetic parameters, and to evaluate in a quantitative fashion the interactions among molecules [2].

In the biomedical field, it is significant the investigation of a cytoskeleton polymer, the microtubule. These highly dynamic particles are involved in various cellular functions, such as movements of the inner cell organelles and intracellular transport. Moreover, they play a crucial role in cellular division. Modifications in microtubule functions, related to specific gene mutations, are responsible of some pathologies, as autosomal dominant microcephaly [3].

The analysis of the dynamic behavior of microtubules in fluorescence microscopy images is a challenging problem, because the particle dimension is below the instruments resolution, that is approximately 100 nm [2], while the microtubules dimension is about 20 nm.

Other challenges are related to the different types of noise and other impairments that corrupt the images (e.g. photon shot noise, background noise, dark current, photobleaching) [1].

Although in the last years several image analysis tools have been proposed for microtubule tracking, due to the complexity of this issue and the lack of a reliable *ground truth*, the biologists still review the samples manually. It is clear that this manual work is time-consuming, hardly reproducible, not so accurate because it is strongly affected by the inter and intra-subject variability. For these reasons automatic analysis is deemed very useful by specialists [2].

In the following sections a brief description of microtubules, their functions and the technique that allow to acquire the images is provided.

1.1 Microtubules

Microtubules (MTs) are one of the three main building blocks of the cytoskeleton, the cellular scaffold that has both functional and structural properties. The cytoskeleton is involved in several processes, such as spatial organization of the cellular organelles, communication with the ECM (Extracellular Matrix), coordination of the signals that aim making the cell move and changing its shape [4].

The cytoskeleton is composed of three kinds of polymers (Fig.1.1):

- Actin filaments;
- Microtubules;
- Intermediate filaments.

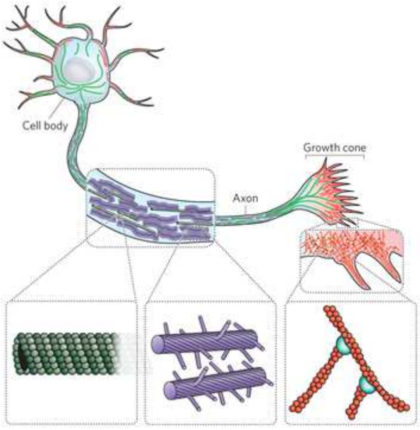

Figure 1.1: The three cytoskeleton building blocks in a neural cell. In details, from the left: microtubules, intermediate filaments, actin filaments. From [4]

These three components build up a network, whose structure is regulated by different regulatory proteins.

In this work we focus on the microtubules, because of their crucial role in eukaryotic cells, especially for maintaining the genome integrity during the mitosis.

1.2 Microtubule structure

The structural elements of the microtubules are dimers of a globular protein, named tubulin. The dimer is composed of two kinds of polypeptides, α-tubulin and β-tubulin. These dimers polymerize into linear protofilaments; 13 of them, arranged around a hollow core into head-to-tail arrays, make up the microtubule (Fig. 1.2).

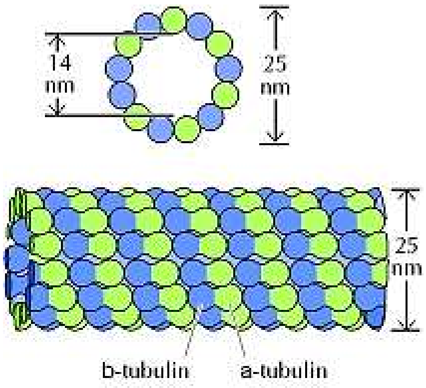

Figure 1.2: α/β dimers arranged around the hollow core. From [5]

Because of their structure, the microtubules are polarized elements and it is possible to recognize two different poles (e*nds*):

- *Plus* end;
- *Minus* end.

The first one is characterized by a fast speed of growth, the latter by a slower one. This velocity difference impacts on the number of free dimers that bound at the two ends, making the growth happen mainly at the plus-end.

The microtubule minus-end is linked to the cell centrosome, located close to the nucleus in interphase cells, while the plus-ends extend toward the cell cortex. In Fig. 1.3 it is shown how the MTs are arranged in the cell during the interphase.

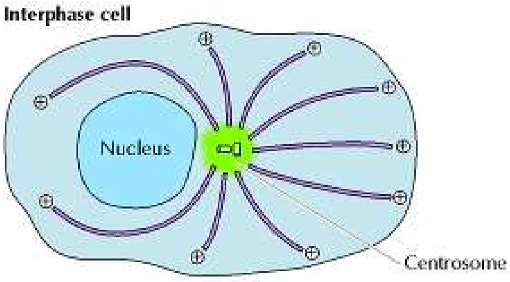

Figure 1.3: Microtubules orientation in interphase cell. From [5]

The dimers can be subject to cycles of assembly (polymerization or *growing*) and disassembly (depolymerization or *shrinking*) regulated by the GTP (Guanosine-5'-triphosphate) hydrolysis. Moreover, the polymerization phase is controlled by a third kind of tubulin, the γ-tubulin [5].

A characteristic microtubule behavior is known as *dynamic instability*, and consists in rapidly alternating phases of growth and shrinkage. The transition from growth to shrinkage is called c*atastrophe*, the opposite is called *rescue.* There is a third state in which a microtubule may be present, the *pause*. It means that the microtubule stops growing but does not depolymerize; unfortunately, the factors that regulate this state are still not fully clear.

This dynamic behavior can be altered by a class of protein selective for the microtubules, the *MAPs* (microtubule-associated proteins). These can have deeply different effects on the microtubule behavior. Some of them are stabilizers because of the capping of the ends, and others act as destabilizers, promoting the depolymerization [5]. In the first case, the MAPs make the polymer mass increase, in the second case they reduce it [3]. A third class of MAPs can be employed as plus-end tracking. These molecules are selective for that pole, therefore they allow to visually check the growing of the MTs. Because of their features, these MAPs are known as *+TIPs* (Microtubule plus-end tracking proteins).

Nowadays, +TIPs are largely used to evaluate the parameters of interest in living cells, and have been employed also in this work for MT tracking.

1.3 Microtubule function

The microtubules are involved in the movement of the inner cell organelles and the intracellular transport, as well as in the cell division, i.e. in the mitosis process.

The microtubule nucleation has a strong impact on the mitotic spindle assembly. This latter is a macromolecule that plays the role of guaranteeing the correct chromosome segregation to two daughter cells during the mitosis [3].

The MTs dynamic instability, during the interphase, causes the cytoskeleton remodeling in order to properly prepare the cell to the division and ensure the genome integrity. During this phase, the microtubules move in the surrounding cellular space for a few micrometers.

Three types of microtubules contribute to the mitotic spindle assembling [3]:

- *Kinetochore MTs* (K-MTs): they link to the chromosomes thanks to a particular protein, called kinetochore;
- *Astral MTs* (A-MTs): they are involved in the spindle orientation and they interact with the cellular cortex;
- *Non-kinetochore MTs* (nK-MTs): they provide stability to the spindle.

These three intracellular molecules give rise to an antiparallel and polarized structure, since the MTs linking centrosomes are arranged in an array fashion, and the ones outside the spindle are arranged radially, with the minus-ends directed toward the centrosome and the plus-ends toward the cellular cortex (Fig. 1.4).

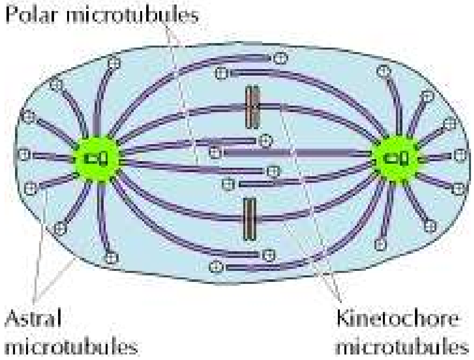

Figure 1.4: Overview of the mitotic spindle. It is shown how the different types of MTs are arranged into the antiparallel array. From [5]

The effectiveness of the spindle assembly is known to be related to the frequency of catastrophe events and to the growth rate of the microtubules, which, on the other hand, is linked to the concentration of free tubulin dimers [3].

When the mitotic spindle is not correctly oriented, due to some gene mutations, abnormal chromosome segregation can occur, and this leads to possibly pathological situations. Focusing on the neural cells, it is significant to mention the *MCPH* (human primary microcephaly), a disorder in which the patients exhibit a reduced head circumference and different degrees of intellectual disability.

1.4 Microtubules detection

The subcellular components and their dynamic behavior can be analyzed *in vivo* using confocal microscopy, a particular kind of microscope based on the fluorescence phenomenon.

Since the cells and their molecules are transparent in normal conditions, in order to detect a specific particle, markers having the property to emit light are used. These molecules are selective for the proteins to detect and are called fluorophores [1].

The fluorescence microscopy, although being a powerful tool allowing *in vivo* imaging of molecular structures, is affected by limitations due both the instrumentation and samples [1]. As consequence, noisy images are generated, whose analysis is very challenging.

More details on main issues related to molecular imaging are provided in the next chapters. In the following paragraphs the basic physic concepts of a confocal microscope are briefly explained, and the fluorophores employed to detect microtubules are described.

1.4.1 Fluorescence

The phenomenon of fluorescence is the capacity of a molecule to release the received radiation. Usually, the excitation and the emission wavelengths are not equal, and their difference is known as *Stoke shift*.

When the radiation is supplied, molecules change their energetic state, which mainly depends on electron configuration, moving from the ground state to a higher-energy condition. Fluorescence occurs when the sample comes back to its steady-state, releasing the received energy in form of photons (quantum of energy) [1].

The wavelength of the radiation and the energy are connected by the Planck's law:

$$E = h \cdot v = h \cdot \frac{c}{\lambda}$$

where:

- E is the photon energy;

- h is the Plank's constant;
- v is the light frequency related to the light speed (c) and the wavelength of radiation (λ).

Because of heat dissipation, not all the excitation energy is emitted in form of photons; this explains the existence of the Stoke shift and the reason why the wavelength of emission is larger than the excitation one.

1.4.2 Confocal microscope

The energy source used for the scanning is a laser. The beam is focused on the sample through a pinhole that limits the quantity of light generated from the source. The diameter of this component is a critical parameter, since it impacts directly on the image resolution. A trade-off must be taken into account, because small pinhole size means better resolution but also less light collected and therefore noisy images [1].

The spatial resolution is expressed by means of the *point spread function* (PSF), which can be considered as the impulse response of the image. In a confocal instrument with a pinhole aperture, PSF is given by [2]:

$$PSF(r,z) = \left| \int_0^1 2J_0(\alpha r\rho)\exp(-2i\gamma z\rho)^2 \,\rho d\rho \right|^2$$

where:

- $r = \sqrt{x^2 + y^2}$ is the radial distance from the optical axis;
- J_0 is the Bessel function of zeroth order;
- α and γ are two parameters depending on the microscope lens numerical aperture (*NA*) and on the emission light wavelength (λ) as follow:

$$\alpha = \frac{2\pi NA}{\lambda} \quad and \quad \gamma = \frac{\pi NA^2}{2\lambda}$$

The PSF in most cases can be approximated with a normal distribution.

To improve the resolution of the system, an immersion layer (e.g. oil) between the lens and the sample is used; in this way, a higher refractive index, and therefore a better resolution, is obtained [1].

The limited resolution (about 100 nm) is not the only factor affecting the image quality. Other phenomena that degrade images are related to both instrumentation and samples, and are: limited SNR (signal-to-noise ratio), variability of the biological samples, photobleaching, autofluorescence and phototoxicity that limit the frequency of excitation in cell imaging *in vivo*.

As a result, the images appear very noisy, and a huge processing is required in order to achieve more reliability in the analysis. Fig. 1.5 shows a typical image acquired with a confocal microscope.

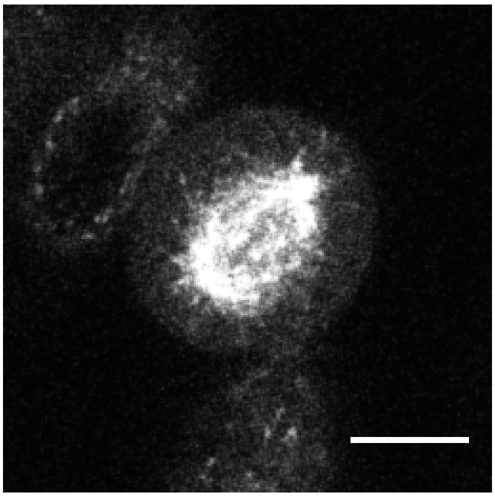

Figure 1.5: A cell in mitotic phase acquired with a confocal microscope with microtubules labelled. Scale bar 10 µm.

1.4.3 Fluorophores

An important step forward into the microscopy field is linked to discovery of a naturally fluorescent protein in living organisms, the *GFP*. Over the years, different fluorophores have been created by inducing GFP mutations. In this way, different genes of interest can be marked, and their behavior can be analyzed, also in a quantitative way [2].

The main feature of the targeting molecules is that they must not affect the cellular functions in any way [1].

By focusing on microtubules, the dynamic is usually studied in time-lapse images (2D images over the time) employing tracers build up with tubulin linked covalently to a fluorophore. Only the MTs growth phase can be monitored using the mentioned above tracers, as, because of their structure, they are selective for the *plus* ends. This is the reason why these are called *fluorescently-tagged End Binding Proteins* (EB-EGFP). In the experiments involving MTs mainly two types of proteins are employed, the type 1 and type 3, called EB1-EGFP and EB3-EGFP respectively.

Since the available number of binding sites for free tubulin decreases exponentially along the microtubule and it is larger at plus end, the polymers fluorescence profile appears in the images as a *comet* (Fig. 1.6) when the microtubule starts the polymerization [6].

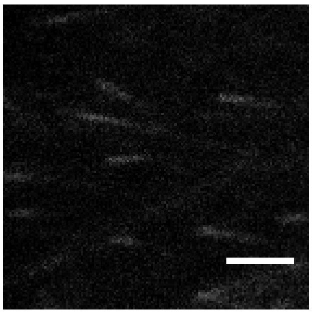

Figure 1.6: Some *comets* marked in the fluorescence images. Scale bar 2 μm.

It is worth noticing that the EB-EGFP markers allow to visualize in time-lapse image sequences only the growing MTs, because they bind to plus-ends in the assembling phase. Other phenomena such as shrinkages and pauses cannot be directly observed.

The cell cultures employed in this work are treated with EB3-tdTomato, a protein belonging to the +TIPs class and therefore selective for the MTs plus-ends.

The comet detection is the starting point for the microtubules analysis software and it is followed by a tracking step. The approaches applied in the currently available tools are the subject of the next chapter.

Chapter 2

Microtubules detection and tracking: state of the art

The detection and tracking of particles in time-lapse fluorescence images have been addressed by many studies, since a quantitative analysis of the reconstructed trajectories yields significant information about functions in living cells [7].

Nowadays, these studies are performed by hand, tracking for each particle its trajectory along the frame stacks. It is clear that this is a challenging and time-consuming job, especially if the number of particles to track is considerably large as in the microtubule case.

In order to support biologists to carry out quantitative and reproducible investigations on time-lapse images, some software tools have been developed.

The purpose of this chapter is to provide an overview of the available approaches for detection and tracking of microtubules. It is worth noticing that nowadays there is no standard protocol to follow because of the extreme variability of the biological process and the equipment used to acquire the sequences of images.

Most algorithms are divided into four main steps [2]:

1) *Data preprocessing* to reduce noise levels;

2) *Segmentation*, that consist in recognizing and sealing off the objects of interest (signals) from the background;

3) *Particle linkage* for tracking the previously identified objects frame by frame;

4) *Results analysis* for providing quantitative information about microtubules dynamic.

An important factor to take into account is that the fluorescent markers have a size under the optical resolution of the microscopes, which is about 100 nm [7].

Moreover, a parameter that impairs the algorithm performance in terms of accuracy, robustness and precision is the extremely low *signal-to-noise ratio* (SNR) (further information is provided in chapter 3. Different researches have independently identified for SNR, specifically in this type of images, a critical value of 4dB. Under this threshold, the reliability of virtually any algorithm quickly impairs [7]. This is the reason why the SNR enhancement is crucial; to this purpose, denoising techniques provide a valid support. Since the predominant noise that corrupts images is not additive, nonlinear filters are used in most of cases [2].

Other problems to tackle are the low contrast of the images due to the limited number of fluorescent markers that bind to the plus-ends, the autofluorescent background [8], and the fact that microtubules might go out from the focal plane during the experiments.

Depending on their features, the existing approaches can be classified into three main classes:

- Probabilistic;
- Deterministic;
- Supervised (i.e. based on machine learning).

In the next sections, for each class, the main features of the algorithms developed for detecting and tracking microtubules are summarized.

2.1 Probabilistic approach

These tracking approaches are based on the implementation of a filter which is based on two types of models, the *dynamic* and the *measurement* model. The first one provides modelling of the spatial-temporal behavior of the MTs (and more in general, of the particles of interest), and the second one includes some measurements in the first model. The purpose of this filter is to predict the particle positions from a series of measurements.

The filtering previously described is often applied through the *Kalman filter* [8]. It is an estimator of the *state* of a linear system corrupted by noise, and works in optimal conditions if the noise and the error that affects the models are two variables normally distributed with mean zero and not statistically correlated. However, surprisingly good results can be obtained even if the ideal working conditions are not respected.

The Kalman filter is a recursive filter based on two steps: prediction and measurement update. Every time a new measure is detected, its reliability is evaluated by comparing the measured value with the prediction yielded by the system model. Through some matrix operations, a weight is assigned to the measure, and the models of the filter are corrected in order to achieve a better estimation in the next epoch.

It is worth pointing out that, to ensure the filter functioning, it is essential to properly establish the particle motion regime (e.g. linear, Brownian or mixed), which represents the evolution of the molecule [8].

A more complex application of the Kalman filter is in the *Interacting Multiple Model* (IMM) filter. It is based on the implementation of a set of Kalman filters to provide a recursive estimation of the model. In this way, more information is retrieved from the "history" model [9].

The third filter that is worth mentioning is the *particle filter*. It is obtained by the implementation of the Monte Carlo method (a class of computational algorithms). This approach is ideal when the models are neither Gaussian nor linear, and ensures a high degree of robustness also when the images are difficult to analyze [8].

A detailed description of the above mentioned filters is out of the scope of this thesis, details can be found e.g. in [8] or [9].

An application of the probabilistic approaches is embedded in the algorithm proposed by *P. Roudot et al.* [9]. Their aim is to recover the particle trajectories in environments with a high density of molecules and subject to rapid motion changes. This scenario leads to an increase in the number of *false positives,* namely objects that have the characteristics to be considered as particles of interest but actually are not. The authors tackle the issue following two strategies [9]:

- Stochastic smoothing;
- Piecewise-stationary motion modeling (PMM).

Their combination is the basis of the *piecewise-stationary motion model smoother* (PMMS) algorithm. What makes this technique innovative is the analysis of both temporal directions in the time-lapse images, so collecting the maximum amount of available information.

The first step plans to detect the particles of interest; therefore, for each pixel, a Gaussian distribution of the PSF is estimated with a fitting procedure, and a threshold of significance is computed from fitting residuals.

In order to estimate the positions of the object centroids, a Gaussian particle intensity model is used. In particular, the coordinates of the pixel previously labeled as significant and those of a local maximum are fit. The searching of the maxima is carried out in an image filtered with a Laplacian-of-Gaussian filter [9]. As for the fitting procedure, a region of interest (ROI) around the significant pixel is considered.

Once the particles have been detected, the next step provides for the tracking and therefore the recovery of the trajectories.

The approach proposed by the authors is an update of an existing multiple-particle tracking software made available in Matlab environment, namely *u-track* [9]. This is done because, if one takes into account only the past information, some motion transitions cannot be predicted (e.g. a rapid switch from Brownian to directed motion).

Focusing on the microtubules scenario, it can be said that the polymers mainly show a linear motion, rarely a Brownian one.

Moreover, an adaptive searching radius for linking particles frame-by-frame is implemented by exploiting both past and future measurements in order to tackle sudden changes.

Once the tracks have been identified, they are optimized in a second step which provides for *gap closing*. This means that the fragmented tracks are properly connected. This process depends on the definition of two parameters: the maximum gap time and the minimum tracks length to take into account.

The PMMS algorithm exploits sets of Kalman filters, each of which is associated to a specific motion regime; the iterations are carried out without mixing the types of motion. The model updating is made in real-time, comparing the new measurement with the other available ones.

If a new motion regime is detected, all Kalman filters are reinitialized with the results of the previous filtering cycle. Since the most recent data on the motion regime are used for the initialization, this represents a suboptimal choice, particularly in the case of rapid changes [9].

The solution proposed by *P. Roudot et al*. exhibits robustness even when the samples present jerky movements and the frames are acquired with a reduced frame rate, choice that allows to reduce the phototoxicity effects and track poorly labeled molecules. This is the reason why the PMMS estimator is a good decision when the objects to detect are characterized by heterogeneous motions.

2.2 Deterministic approach

This category of algorithms follows a procedure that can be divided into two macro steps: the localization of particles through enhancing techniques, and the reconstruction of trajectories based on a nearest-neighbor criterion [8]. Generally, the concept of *near* should not be regarded only referred to space, but also to pixel intensity, shape, direction and other relevant aspects.

The majority of approaches implement a search strategy which exploits the intensity of the pixels; in particular, the positions of the molecules correspond to those of the peak intensity.

Thresholding techniques to detect particle positions are applied by *I.F. Sbalzarini and P. Koumoutsakos* in [10]. In contrast with other algorithms that can be found in literature, the approach proposed in [10] foresees few *a priori* knowledges, and no assumptions on the shape of trajectories are required. Nevertheless, the technique is characterized by accuracy and precision comparable with trickier algorithms, and has benefits also from a computational standpoint [10], even if this feature is not really relevant to the purpose of this work.

In the initialization phase, all pixels of the sequence are normalized with the min-max scaling; maximum and minimum values of intensity are referred to the entire stack.

Then, image enhancing is performed in order to reduce two noise sources: the long-wavelength modulations of background intensity, and the discretization noise that affects the digital images (i.e. photon shot noise) [10]. To this end, two low pass filters (LPF) are used, an average filter to remove the background and a Gaussian filter to limit the discretization noise. The first one is based on the assumption that the objects of interest have limited variations compared with the background, therefore a box-car average in a square ROI is implemented. As for the second filter, a normal distribution is assumed for camera noise.

The filtered images are the starting point for particle identification. For each of them, the local maximum is evaluated in order to estimate the object positions.

This approach has two main limitations [10]:

1. It does not exclude noise;
2. It can include false positive particles.

For reducing these problems, a refinement of the positions and the removal of spurious identifications are required.

To this aim, the authors fix the particles location, making the assumption that the local maxima detected should be not so far from the real geometric center of the object. An offset is the value that allows to correct the particles coordinates, and it is represented by the distance to the brightness-weighted centroid in the image.

The false detections are rejected by assigning a score depending on the intensity profiles.

Once the particles positions are estimated in all frames, they are linked frame-by-frame to build up the trajectories. To this purpose, a nearest-neighbor criterion is employed. The linking of two particles p and q through two consecutive frames i and j, is based on the minimization of a cost functional, defined as a linear combination of the particle positions, the intensity moments of zeroth (m_0) and second order (m_2) [10]:

$$\phi_{ij} = (\bar{x}_{p_i} - \bar{x}_{q_j})^2 + (y_{p_i} - \bar{y}_{q_j})^2 + (m_0(p_i) - m_0(q_j))^2 + (m_2(p_i) - m_2(q_j))^2$$

This approach provides good results and is very efficient from a computational point of view [8]. This is the reason why it has been taken as reference in several works over the years, such as the one developed by *Sironi et al.* and also in this thesis. However, the performance impairs when the images exhibit low quality, and in display environments with a high density of particles, that is the situation addressed in this work.

2.2.1 Combined approach

In some cases, it is possible to mix both the above mentioned approaches. For example, it is worth mentioning the solution proposed by *B. Mahemuti et al.*, which investigate the microtubules dynamic using morphological information for detection and a *probabilistic data association* (PDA) filter for tracking.

The algorithm reported in [11] starts with the binarization of the images belonging to the movie to analyze, and the removal of all the objects shorter than a threshold depending on the minimum length of microtubules to detect. This parameter impacts the tracking accuracy.

Then, the elements identified undergo thinning procedure in order to have microtubules 1 pixel wide [11].

The next step provides for the plus-ends identifications in the binarized images and is based on the assumption that the body of MTs follows the path of head (i.e. plus-end). Taking into account this hypothesis, two consecutive frames will be different just for the positions of the growing ends, and therefore the result of subtracting the two frames is an image containing only the heads of the microtubules.

Moreover, since some tracks might cross during the polymer growth, a procedure of objects decomposition is performed in order to isolate single particles forming compound structure. To this purpose, information related to the plus-end positions, the crossing points, and the pixels are exploited.

Once the microtubules positions are estimated, the tracks are created with a probabilistic approach considering that the objects could change their shape and topology in different frames of the same video, or that some MTs can suddenly appear or go out from the focal plane. The authors consider the elements into consecutive frames as belonging to the same microtubule if the measured and estimated positions are similar in direction and movement. The PDA filter is based on the Kalman filter, and follows two steps: data association and track updating.

The described technique is characterized by acceptable accuracy in environments with low density of particles; however the performance impairs in high density video, that is the most realistic situation.

2.3 Approach based on machine learning

Machine learning is a powerful tool that allows building up specialized algorithms taking into account the morphology and physic of phenomenon without any *a priori* knowledge of the particles to analyze.

This is possible because the algorithm *learns* from a collection of data, termed *training set*. It means that each track in an image is considered as an observation instance and, from the observation of different tracks, it is possible to build a behavior pattern.

Once the *training* procedure is over, the algorithm can evaluate the dynamic of the particles in the movies of interest.

However, in the biological field, machine learning is not the most appropriate choice because of the nature of the objects behavior. Indeed, it is a random process, as in the microtubules case, that leads to the lack of a *ground truth* to use for the *training* of the

algorithm. To build an appropriate dataset for the learning procedure, a very comprehensive study of the motion model of the microtubules would be needed.
To create such simulator for generating the training set, costs comparable with those of a manual analysis are required.
This explains why, even though the huge potential of the machine learning, at present traditional approaches remain the best choice for molecular images evaluation.

In conclusion, it is worth pointing out that regarding the particle detection and tracking, at present, there is not the best algorithm, because the performance of any method is linked to the experimental dataset. For this reason, the approach to implement should be chosen according to the available dataset.

Chapter 3

Dataset description

The purpose of this thesis is to provide an algorithm for detecting and tracking astral MTs in a fully automated way and supply a summary of their dynamic behavior in order to support biologists in research. For the algorithm testing, a dataset of stacks (i.e. time-lapse image sequences), acquired with a confocal microscope, has been supplied by the Department of Molecular Biotechnology and Health Sciences of Turin.

Moreover, cells have been treated with two different drugs, nocodazole and taxol, in order to theoretically control their behavior. However, in practice, because of the several factors that affect cell functions, alterations are not so easy to interpret.

The used drugs have opposite effects on MTs dynamic, since nocodazole promotes the MTs disassembly, while taxol the assembly. This is the reason why nocodazole is referred to as “MTs destabilizer” and taxol as “MTs stabilizer”. Both agents can be helpful in the treatment of different kinds of cancer, because, at specific concentrations, they block the mitosis, thereby limiting tumor proliferation [12].

It is worth noticing that the alterations of MTs dynamic are dose-dependent; this is the reason why the cells were doped with different drug concentrations.

Moreover, *control* stacks have been regarded as reference since, in those movies, MTs dynamic is not affected by drugs.

This chapter aims to describe the data from a biological and technical standpoint.

3.1 Cell culture

HeLa-K (HeLa Kyoto) cell line, expressing EB3-td Tomato, was chosen to carry out the experiments and acquire movies. HeLa is a particular cell line often used in scientific research, and is the first human cancer cell line immortalized in tissue culture. They were named “HeLa” after Henrietta Lacks, a woman that was affected by adenocarcinoma of the cervix, from which cells were extracted with a biopsy [13].

Cell culture was maintained in DMEM-GlutaMAX (Invitrogen) medium supplemented with 10% fetal bovine serum (FBS), 100 U ml^{-1} penicillin, 100 μg ml^{-1} streptomycin, 200 μg ml^{-1} Geneticin (Sigma) and 0.5 μg ml^{-1} puromycin.

Interphase cells were treated with nocodazole and taxol drugs, and, after 1 h, videos of astral MTs have been acquired. In detail, imaging process was performed using a Leica TCS SP5-AOBS 5-channel confocal system equipped with a 561 nm DPSS laser. During the acquisition, cells were stored in the microscope incubator at 37°C with 5% of CO_2. Videos were recorded with a sampling period of 0.5 s for 2 minutes.

3.2 General information and parameters

The experimental dataset can be divided into two groups: the first one includes all stacks treated with nocodazole, and the other one cells doped with taxol. For both drug types, four increasing drug concentrations have been taken into account.

In the nocodazole case, the tested concentrations were:

- 0 nM (*control stack*);
- 1 nM;
- 10 nM;
- 100 nM.

The taxol stacks were treated with the same doses of the nocodazole, except that, instead of 1 nM, a concentration of 0.1 nM was considered.

For each dosage, in both cases, five stacks have been acquired and saved in TIFF format. The only exception is the number of stacks related to taxol at 0.1 nM; they are six instead of five.

From a technical standpoint, all movies share the same features:

- Frame size: 256x256 pixels;
- Number of frames for each stack: 120;
- Frame rate: 2 fps (frames per second);
- Pixel resolution: 64 nm;
- Bit depth: 8;
- Color type: grayscale;
- Display range: 0-255.

3.3 Noise description

In this section the main phenomena degrading the quality of confocal images are described. Noise, in this scenario, is mainly due to two sources. On one side, the equipment induces errors in measurements and in data quantization; on the other side, the sample itself affects image quality [1].

One of the main types of noise that impairs images is known as *photon shot noise* or *Poisson noise*. It is due to the random emission of photons [1]. As it comes out from its name, the impact of photons on the detector follows a Poisson distribution.
This is an electronic noise that becomes relevant when the number of photons is so small that the uncertainty related to the Poisson distribution cannot be longer neglected [14].
Noise intensity is proportional to the square root of the average number of events N (i.e. light intensity). Signal-to-noise ratio, in an image corrupted by shot noise, is [14]:

$$SNR = \frac{N}{\sqrt{N}} = \sqrt{N}$$

In the previous formula the denominator represents the noise standard deviation.
It is clear that, in a Poisson-distributed function, SNR matches with the square root of the number of events. Moreover, noise levels are stronger when the light source has a reduced intensity and decrease when N is very large [14].

However, the source cannot have a high intensity because of *photobleaching*; it means that the markers lose their capability to fluoresce if they are intensively stimulated. The problem is related to the light intensity, and also to the experiment duration. In order to limit the effects of this phenomenon, the exposure time and the light intensity should be maintained at low levels [1].

It is worth mentioning also the presence of *speckle noise*; it is a multiplicative noise that degrades images, making them look visually grainy. It becomes relevant when coherent imaging systems are employed, such as laser in confocal microscopy. Noise, in this case, is caused by random interferences between the coherent returns. The effect on grayscale images is an increase of mean intensity in a local area [14].

Another noise source, related to samples, is the a*utofluorescence*; it is due to fact that some molecules naturally fluoresce at wavelengths in the range of visible spectrum. This emission overlaps with the fluorophore one, and makes the detection challenging. To make matters worse, the experiments are carried out with a low intensity of excitation [1] because of the reasons previously explained (e.g. photobleaching).

There are other interference sources that degrade confocal images, such as *background noise,* caused by the ambient radiations; *dark current,* due to the thermal agitation of particles at high temperatures inside the detector, which leads to spontaneous emissions; *quantization noise* of the digital output; *scattering* of light, which occurs when the object dimensions are comparable with wavelength size [1].

All the above mentioned interferences lead to a decrease in the overall image contrast and resolution. Fig. 3.1 shows noise effects in a confocal image.

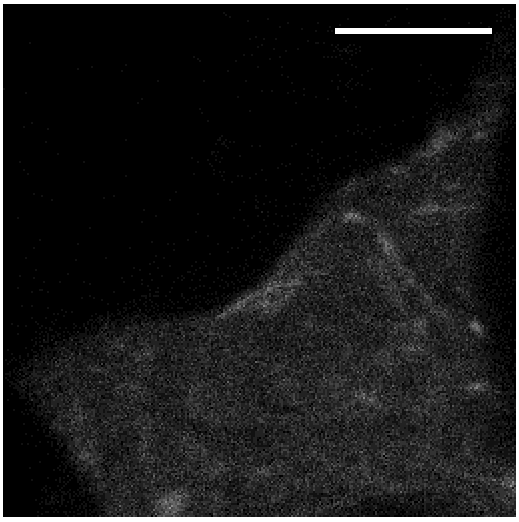

Figure 3.1: Noise effects on confocal image.

Scale bar 5μm.

All stacks used to test the algorithm are made up of frames similar to that displayed in Fig 3.1.

As it is clear from Fig. 3.1, it is difficult to isolate microtubules from the surrounding environment since signal levels are comparable with the background ones.

It is worth pointing out that particle positions can be detected with an accuracy related to the pinhole detector as follows [2]:

$$\epsilon = \frac{\sigma}{\sqrt{N}}$$

Where:

- σ is the standard deviation of the PSF approximated as Gaussian;
- N is the number of photons detected in the exposure time.

The interference sources could be limited by choosing a small pinhole diameter detector, even if this limits signal intensity. On the other hand, a large diameter will prevent from obtaining the optical confocal effects and other noise sources will be introduced into the videos. Hence, the tradeoff is to set an optimum aperture for the pinhole detector in order to allow signal detection and, at the same time, reject the main noise sources.

To improve stack quality and reduce noise levels, all movies have to be managed with image processing techniques.

3.4 Statistical analysis

3.4.1 Signal-to-noise ratio

SNR is a parameter strictly related to the algorithm performance. The most common definition employed in the biomedical field is a differential one, i.e. the difference between the mean intensity of the object and background divided by the background standard deviation:

$$SNR_d = \frac{\bar{I}_{object} - \bar{I}_{background}}{\sigma_{background}}$$

As already mentioned, it is recognized that, if the SNR defined in the previous formula, is below the value of 4 dB, the performance of any algorithm is seriously impaired [7].

In table 3.1 the SNR values related to the stacks employed in this work are summarized.

NOCODAZOLE		
Dose	Stack ID	SNR_d
0 nM	Ctrl 003	4.47
	Ctrl 005	3.80
	Ctrl 011	6.90
	Ctrl 013	6.23
	Ctrl 015	4.31
1 nM	Series 002	1.14
	Series 005	3.52
	Series 007	5.31
	Series 012	4.76
	Series 015	4.76
10 nM	Series 003	5.31
	Series 005	4.62
	Series 008	1.55
	Series 011	3.22
	Series 014	1.96
100 nM	Series 002	2.58
	Series 004	4.01
	Series 006	3.96
	Series 009	2.01
	Series 011	5.31

TAXOL		
Dose	Stack ID	SNR_d
0 nM	Resonant	2.46
	Ctrl 018	3.58
	Ctrl 024	3.52
	Ctrl 028	3.94
	Ctrl 031	3.36
0.1 nM	Series 003	2.28
	Series 006	4.07
	Series 010	3.58
	Series 015	5.29
	Series 018	6.48
	Series 025	4.03
10 nM	Series 006	6.47
	Series 009	1.67
	Series 012	3.16
	Series 015	3.60
	Series 018	1.37
100 nM	Series 002	2.30
	Series 008	1.88
	Series 011	3.01
	Series 016	1.24
	Series 019	0.49

Table 3.1: SNR_d (dB) values of the stack belonging to dataset.

From the results, it is clear that a trend cannot be identified; hence the dataset shows an extreme variability in noise levels. All stacks are affected by noise, but, considering only SNR_d values, cells treated with taxol at 100 nM seems to be more affected. Since most original frames are characterized by values below the critical threshold (or just above it), denoising is required in order to increase the SNR_d, thereby improving the algorithm reliability.

3.5 Spectral analysis

Analysis in the frequency domain allows one to understand what kind of noise corrupts images. The image spectrum is helpful in order to plan the denoising process.

3.5.1 Two-dimensional Fourier Transform

One-dimensional Fourier Transform concepts can be extended to the 2D case. Taking into account a digital image *x(m,n)* with dimension *M*×*N*, the analysis and synthesis equations can be respectively written as:

$$X(\mu, \nu) = \sum_{m=0}^{M-1} \sum_{n=0}^{N-1} x(m,n) e^{-j2\pi(\mu m+\nu n)} \qquad \mu \in \mathbb{R}, \qquad \nu \in \mathbb{R}$$

$$x(m,n) = \int_{-\frac{1}{2}}^{\frac{1}{2}} \int_{-\frac{1}{2}}^{\frac{1}{2}} X(\mu, \nu)\, e^{j2\pi(\mu m+\nu n)} d\mu\, d\nu \qquad m = 0, \dots, M-1, n = 0, \dots, N-1$$

The parameters μ and ν are spatial frequencies in vertical and horizontal directions, respectively, and $X(\mu, \nu)$ is the 2D spectrum of image $x(m, n)$.

Frequency is related to intensity variations; low frequencies match regions which exhibit slow variations (e.g. background), while high frequencies are associated to regions characterized by a significant variability (e.g. edges and discontinuities).

The spectrum $X(\mu, \nu)$ is periodic with unitary period for both variables μ and ν, so it is enough to consider one period to display the spectrum.

The range $-\frac{1}{2} \leq \mu, \nu < \frac{1}{2}$ is usually set in order to have low frequencies located around the origin of axis.

Moreover, an enhancement of dynamic is required with a view to better displaying the amplitude spectrum. This operation is carried out with a logarithmic operator using the formula below:

$$|X(\mu,\nu)|_{en} = 10 \cdot \log_{10}\left(\frac{|X(\mu,\nu)|}{\max(|X(\mu,\nu)|)}\right)$$

By applying the above mentioned procedure to an image belonging to the available dataset, the spectrum appears as in Fig 3.2a.

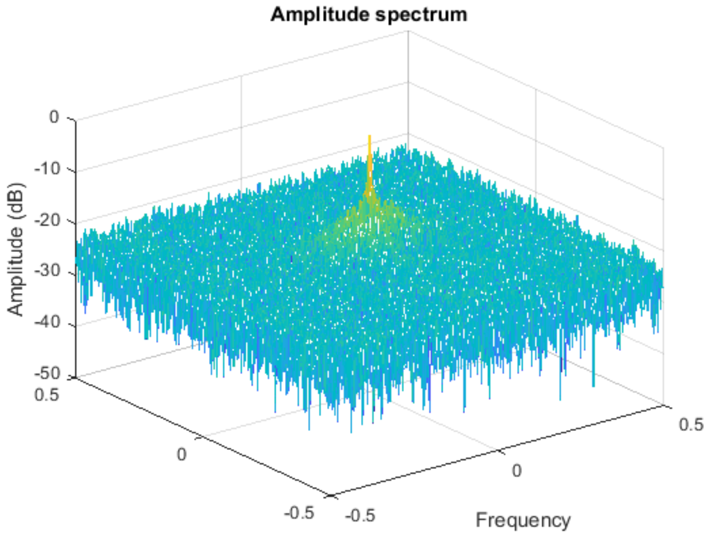

(a)

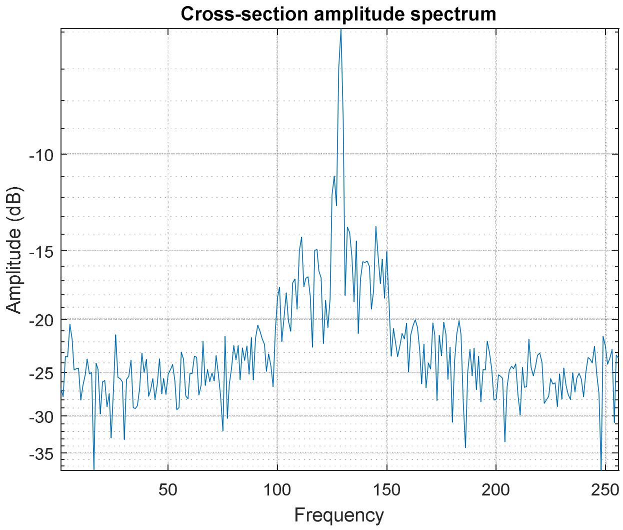

(b)

Figure 3.2: Amplitude spectrum of nocodazole stack *ctrl 013*.
(a): 2D FFT module. (b): cross-section of the same spectrum.

From Fig 3.2a, it can be noticed that the signal exhibits a low-pass behavior since its distribution is centered around the origin of the axis, namely low frequencies.

Moreover, it is worth noticing that signal is surrounded by noise whose spectrum is basically constant. This is the reason why the noise process can be approximated by *white noise* and as such it will be treated in order to improve images quality.

Chapter 4

Algorithm implementation

The algorithm was developed, as standalone software, in Matlab R2017a and belongs to the deterministic approach category, already described in chapter 2. Hence, the whole pipeline can be divided into two steps: detection and tracking of MTs. In addition, a denoising procedure was implemented in order to reduce noise levels. This phase precedes the real stack analysis, so it is placed at the beginning of the algorithm.

In the next sections, each step, underlying the developed program, is described in detail.

4.1 Algorithm calibration

The algorithm encompasses a preparatory phase of calibration, whose aim is to compute a threshold depending on image intensity. This parameter enables true particles to be recognized. This step is necessary because of the high variability of image intensity among different acquisitions.

For this purpose, a control stack is chosen by the user in order to analyze samples belonging to the same experiment. This choice was made because, in those stacks, cell functions are not altered by drugs and so they can be considered as reference.

Calibration is made by identifying the maximum intensity value throughout the stack selected by the user. Once this value is detected, the final threshold is computed as p percent of that global maximum.

The percentage was set to 35% after a tuning procedure. The algorithm has proven robustness to different percentages, so a value allowing detection of a significant number of tracks was chosen (a hundred tracks in control stacks).

This parameter is used in the next phase of microtubule detection.

4.2 Denoising

As already discussed, $\mathrm{SNR_d}$ values are lower than the critical threshold in many samples. This is the reason why the denoising procedure has been designed to improve that parameter, making more reliable the subsequent steps. To this purpose, given the statistic of noise process, a LOG-Wiener Transform has been implemented.

4.2.1 Wiener filter

This is a linear filter often used for image denoising, and it is based on two main assumptions:

- Noise and signal are not correlated;
- Noise is an additive random process.

According to the second hypothesis, an image corrupted by noise can be modelled as follows [15]:

$$x(i,j) = s(i,j) + v(i,j)$$

where:

- $x(i,j)$ is the observed blurred image;
- $s(i,j)$ is the original image (uncorrupted);
- $v(i,j)$ is the additive noise (*white noise* in ideal conditions).

The purpose of Wiener filter is to estimate the original image $s(i,j)$ adopting a Bayesian approach. The procedure is carried out by minimizing the mean square error between the uncorrupted and the estimated image ($s(i,j)$ and $\hat{s}(i,j)$ respectively), defined as [15]:

$$e^2 = \frac{1}{N \times M} \sum_{i=0}^{N-1} \sum_{j=0}^{M-1} \left[\left(s(i,j) - \hat{s}(i,j) \right)^2 \right]$$

In order to describe the filtering process and simplify notation, the one-dimensional case is treated. However, concepts can be easily extended to the two-dimensional case. Assuming that we consider a linear system, with unit sampling response $h(n)$, the output to the input signal $x(n) = s(n) + v(n)$, can be modelled as [15]:

$$y(n) = \hat{s}(n) = x(n) * h(n) = [s(n) + v(n)] * h(n)$$

As it follows from the previous formula, the ideal result $y(n)$ is approximated to the estimate signal $\hat{s}(n)$ after the filtering process.

Moreover, it is worth pointing out that the filter works in optimal conditions if noise and signal have spectra that do not overlap in frequency. However, acceptable results can be obtained even if this condition is not satisfied.

4.2.2 LOG-Wiener Transform

It is not effective to directly apply Wiener filter on the images belonging to our dataset, since the underlying hypotheses are not satisfied.

The first problem is that the Poisson noise is correlated to the signal and the speckle noise is multiplicative. In order to limit these issues, a LOG-Wiener Transform was implemented.

It consists of three steps to apply to the image:

1. Logarithmic transformation (base 10 was chosen);
2. Application of Wiener filter;
3. Inverse logarithmic transform (with the same base chosen in the step 1).

The idea underlying the proposed technique is that, by applying a logarithmic operator, multiplicative noise will be processed into an additive one. However, noise process is additive but not necessarily Gaussian.

Table 4.1 summarizes how SNR_d values changed once stacks were processed with LOG-Wiener Transform.

NOCODAZOLE			
Dose	Stack ID	$\mathrm{SNR_d}$	$\mathrm{SNR_{dLW}}$
0 nM	Ctrl 003	4.47	7.16
	Ctrl 005	3.80	4.91
	Ctrl 011	6.90	8.13
	Ctrl 013	6.23	7.92
	Ctrl 015	4.31	6.53
1 nM	Series 002	1.14	6.02
	Series 005	3.52	5.77
	Series 007	5.31	5.88
	Series 012	4.76	8.75
	Series 015	4.76	6.33
10 nM	Series 003	5.31	6.90
	Series 005	4.62	9.82
	Series 008	1.55	2.70
	Series 011	3.22	10.79
	Series 014	1.96	2.07
100 nM	Series 002	2.58	4.62
	Series 004	4.01	7.60
	Series 006	3.96	5.71
	Series 009	2.01	10.79
	Series 011	5.31	5.68

TAXOL			
Dose	Stack ID	$\mathrm{SNR_d}$	$\mathrm{SNR_{dLW}}$
0 nM	Resonant	2.46	5.07
	Ctrl 018	3.58	4.79
	Ctrl 024	3.52	5.26
	Ctrl 028	3.94	6.81
	Ctrl 031	3.36	7.92
0.1 nM	Series 003	2.28	3.18
	Series 006	4.07	5.73
	Series 010	3.58	6.87
	Series 015	5.29	6.52
	Series 018	6.48	7.06
	Series 025	4.03	4.77
10 nM	Series 006	6.47	8.09
	Series 009	1.67	4.28
	Series 012	3.16	3.67
	Series 015	3.60	6.72
	Series 018	1.37	3.80
100 nM	Series 002	2.30	3.96
	Series 008	1.88	5.67
	Series 011	3.01	4.77
	Series 016	1.24	2.04
	Series 019	0.49	3.67

Table 4.1: $\mathrm{SNR_d}$ (dB) values comparison before and after the LOG-Wiener Transform.

The LOG-Wiener Transform has different effects on samples. This is because, given the complexity of noise process, this operation is not always the most appropriate choice. Indeed, because of different types of noise that corrupt images, the working assumptions on Wiener filter are not always fully satisfied.

The filtering effect on some samples is proof of this; e.g. *series 016* of taxol at 100 nM, where SNR_d value stays below the critical threshold of 4 dB, even though the filtering process. Another aspect to note is the effect of filter on *series 009* of nocodazole at 100 nM; in this stack a significant increase of SNR_d can be observed.

Unfortunately, a significant improvement in SNR_d does not always mean a correspondent improvement from an algorithmic standpoint.

However, it is worth noticing that an enhancement of SNR_d can be found in all cases, even if the parameter does not increase equally among the different samples.

Fig 4.1 displays how a frame looks like once LOG-Wiener Transform was applied.

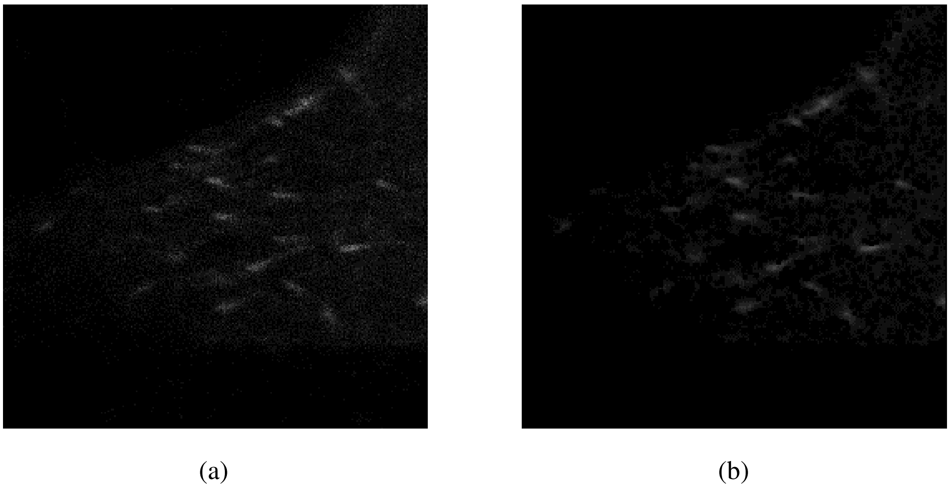
(a) (b)

Figure 4.1: Effect of LOG-Wiener Transform on nocodazole control stack 005. (a): Original frame. (b): Filtered frame.

Fig 4.1b exhibits an overall intensity reduction, but background appears smoothed, if compared to Fig. 4.1a. The uniformity will facilitate the following comet identification.

4.3 Particle detection

Once noise levels have been reduced, the particles can be detected over the frames. In order to limit the false positive rate, an object is recognized as a comet if and only if it exceeds a threshold depending on the intensity of each stack under consideration.

The identified particles are linked over the frames in order to build up the final trajectories, enabling MTs dynamic evaluation.

This paragraph is focused on the implementation of MTs detection procedure in the developed software.

4.3.1 Comet detection threshold

The detection step begins with the evaluation of a threshold that enables comets to be recognized over the frames. In order to avoid false positives, this parameter has to be sufficiently selective, but, at the same time, false negative rate has to be limited.

In detail, the threshold was computed as x times the standard deviation of a frame (x=100). This is because standard deviation is a parameter that suggests the global noise level of the image.

Moreover, noise level is checked in order to recognize stacks below the critical SNR_d value.

If this condition is detected, the algorithm stops working on that stack and a message arises to notify the user.

4.3.2 Local maxima searching

In each frame, comet positions are associated to the peak intensity of those regions that are regarded as microtubules.

Due to the extreme variability of the intensity profile, the search is carried out locally, namely analyzing some ROI with a fixed size. The procedure is performed through a squared sliding window (size 7x7 pixels was set [16]) applied to the filtered image, and covering each frame of the stack. Within each window, the local absolute maximum is detected and considered as a plus-end if its intensity exceeds *n* times the standard deviation of the current frame (*n* is the threshold computed as described in paragraph 4.3.1).

Comet positions are refined by centering the squared window on the local maxima previously detected, and recalculating the peak intensity exploiting the selected neighbor. This step limits the problem of recognizing as split two particles belonging to the same microtubule.

Indeed, window size is related to the minimum distance at which two particles can be detected. Since stack pixel resolution is 64 nm, in stacks belonging to the dataset, it means that minimum peak displacement is 448 nm.

Finally, each peak intensity is compared with the threshold computed in the calibration phase (see paragraph 4.1) and the position is kept if it is above that value, otherwise the maxima coordinates are removed.

Fig 4.2 shows an example of microtubule plus-ends detected after the described process.

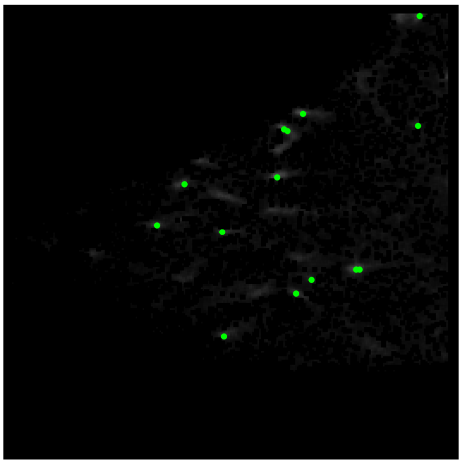

Figure 4.2: Comets detected in frame 6 of nocodazole 005 control stack.

The selected parameters allow to recognize, for each frame, a number of particles of a few dozens, a value established after a discussion with expert biologists which carry out manual detection. This value prevents false positive objects to be detected, even if some real MTs are lost. However, this does not significantly affect the final stage of MTs dynamicity evaluation.

4.4 Microtubule plus-end tracking

Once the particles are identified, they are tracked; it means that object position is monitored over the frames and its coordinates are linked in order to build up a trajectory. All constructed tracks enable the evaluation of features related to MTs dynamic (e.g. velocity, track length, lifetime).

The tracking stage can be divided in two phases, as proposed also in [16]:

1. Partial tracks identification;
2. Final tracks recovery.

4.4.1 Partial tracks

The partial trajectory detection process is based on the *a priori* assumption that microtubules show a rectilinear motion regime. Moreover, movements in the forward direction are taken into account, since the backward ones cannot be directly observed.

The linking algorithm applies a nearest-neighbor criterion. Therefore, plus-end coordinates are connected frame-by-frame minimizing a cost functional based on that proposed in [10] and simplified in [16] as indicated below:

$$\phi_{ij} = (X_{ti} - X_{t+1\,j})^2 + (Y_{ti} - Y_{t+1\,j})^2$$

where:

- X_{ti} (Y_{ti}) is the *x* coordinate (*y* respectively) of the *i*-th particle in the *t*-th frame;
- $X_{t+1\,j}$ ($Y_{t+1\,j}$) is the *x* (*y*) coordinate of the object *j* in the frame *t+1*.

This functional, defined as a linear combination of the particle positions, is related to the global Energy (ϕ) of two molecules, *i* and *j*, belonging to two consecutive frames [16].

Moreover, in order to connect particles, another condition must be satisfied. Between consecutive frames, plus-ends can have a maximum displacement of 7 pixels (448 nm). This critical parameter enables to recognize and link particles belonging to the same trajectory. Algorithm performance is closely related to this parameter, therefore it must be chosen carefully.

As an example, Table 4.2 shows how MTs velocity changes varying the critical distance. The maximum displacement was set on the basis of control stacks, since cell behavior was not altered by drugs. Moreover, only speed values have been reported since this parameter is the most meaningful for microtubule dynamic considerations.

NOCODAZOLE *Ctrl*		
Distance (pixel)	velocity (μm/min)	σ velocity
7	14.99	7.88
6	13.95	7.09
5	13.00	6.55
4	11.15	5.35

Table 4.2: Comparison of mean velocity values of nocodazole control stacks at different distances.

Table 4.2 summarizes the mean values, and their standard deviations, of nocodazole control stacks (the same trend can be found in the taxol case). It can be noticed that both standard deviation and speed go down when distance decreases. Since extremely low velocity values are not common in non-doped cells, a distance equal to 7 was set in the algorithm. Moreover, these values are expected in control cell samples, and are consistent with those reported in literature, e.g. in [16].

Fig. 4.3 exhibits how partial tracks are built up over the frames.

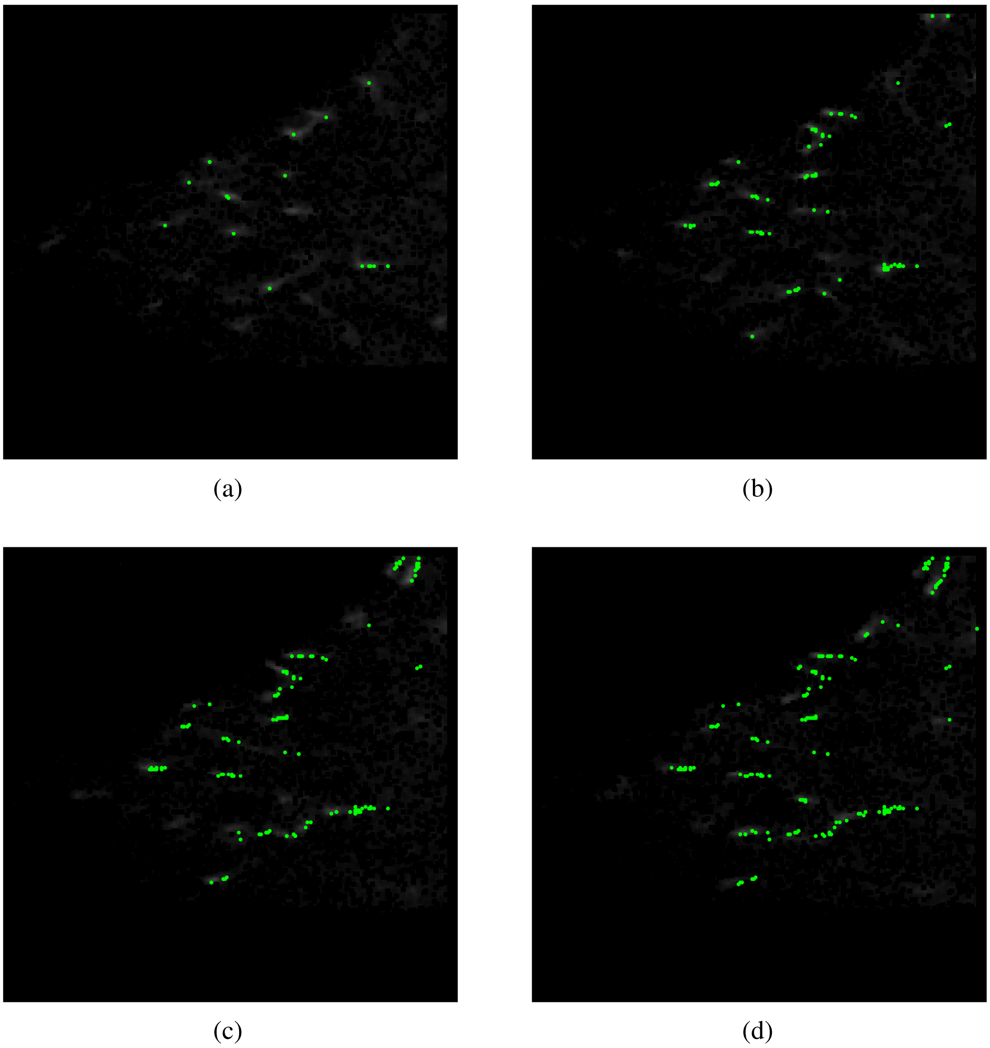
(a) (b) (c) (d)

Figure 4.3: Tracking process on nocodazole control stack 015 at different time points. (a): frame 2. (b): frame 6. (c): frame 10. (d): frame 14.

Once partial trajectories have been identified, in the subsequent step some of them are linked in order to construct the final tracks.

4.4.2 Final tracks reconstitution

This final step was implemented in order to take into account those particles that disappear and then appear again a few frames ahead. This avoids considering as different trajectories actually belonging to the same comet because of *pause* events, which are typical of MTs behavior.

Two trajectories are connected if only two conditions are satisfied:

- The end of the first track and the beginning of the second one lie within a radius equal to the critical distance (described in paragraph 4.4.1);
- The maximum time lapse between two partial tracks is 5 frames (2.5 s) [16].

Once partial tracks have been linked, their coordinates were fitted with a second-degree polynomial. Fitting procedure aims to smooth trajectories, thus limiting rapid changes in the comet shape, that are incompatible with the motion model assumed.

The tracks built up in this way are considered during the evaluation of microtubule dynamic.

4.5 Microtubule dynamic analysis

This phase determines, in a quantitative fashion, all the required information on microtubule behavior.

It is worth pointing out that not all the identified trajectories are taken into account for the parameter calculation. This is the reason why a track screening procedure precedes the actual dynamic evaluation.

4.5.1 Tracks screening

In this stage all tracks shorter than 2.5 s (i.e. 5 time points) are removed. This threshold was chosen in order to avoid considering comets which exhibit Brownian motion. These trajectories are not relevant for considerations on microtubule behavior.

In order to properly remove tracks, the number of time points was set after a tuning procedure. In particular, three values were tested: 3, 4 and 5. The obtained results, for nocodazole stacks, are summarized in table 4.3.

NOCODAZOLE							
Dose	TimePoints	v	σ_v	λ	σ_λ	τ	σ_τ
0 nM	5	15.000	7.885	1.299	0.762	4.915	2.220
	4	14.972	8.070	1.148	0.700	4.279	2.071
	3	15.054	8.023	0.914	0.602	3.419	1.738
1 nM	5	14.699	6.994	1.057	0.415	4.312	1.343
	4	14.340	6.817	0.757	0.355	3.291	1.037
	3	14.830	6.678	0.720	0.332	2.702	0.866
10 nM	5	17.371	7.666	1.175	0.621	4.283	1.364
	4	16.912	7.916	1.013	0.588	3.906	1.365
	3	16.584	7.494	0.712	0.413	3.017	1.221
100 nM	5	12.820	7.455	1.068	0.570	4.613	1.545
	4	11.060	3.534	0.653	0.213	3.250	0.719
	3	10.230	2.534	0.461	0.156	2.612	0.496

Table 4.3: Comparison of parameters related to microtubule dynamic varying the number of time points. v is the velocity (µm/min); λ is the track length (µm); τ is the track lifetime (s). All values indicate the average among the stacks treated with the same drug dose.

It can be seen that speed is little biased by the minimum duration of a track. This can be explained by the fact that, when time points decrease, most of newly detected particles are characterized by Brownian motion. This is the reason why, failing to respect the motion model assumed, they are discarded anyway.

Instead, both length and lifetime decrease reducing the minimum number of consecutive frames in which an object must be detected. This happens because the new particles are shorter and last less.

This feedback was possible because velocity, length and lifetime were computed independently.

In view of the above, the time point number was set to 5 (since it can be inferred that all the removed particles fluctuate for a little while).

Finally, it is worth pointing out that, in this phase, spurious particles, which can be considered as false positive objects, are automatically removed since no trajectory can be identified for them, because they are too short to be evaluated.

4.5.2 Parameter calculation

Once final tracks are available, all parameters, that enable to understand microtubule behavior, can be computed. The algorithm was designed in order to provide mean values of velocity, length and lifetime and their standard deviations.

The instantaneous velocity (in $\mu m/min$), namely velocity between two consecutive frames, was computed as:

$$v = \frac{d \cdot PR}{dt \cdot c}$$

where:

- d is the distance covered by a particle (*pixel*);
- PR is the pixel resolution (*nm*);
- dt is the sampling period (s);
- c is a conversion factor (in order to express velocity in $\mu m/min$).

The global track speed is given by the mean of all the instantaneous velocity values.

Track length (in μm) is calculated as:

$$\lambda = \frac{\bar{d} \cdot PR \cdot TP}{c}$$

where:

- $\bar{d}$ is the average of all instantaneous displacements (*pixel*);
- PR is the pixel resolution (*nm*);
- TP is the number of time points the microtubule lives;
- c is a conversion factor (in order to express λ in μm, it was set to 1000).

The last parameter, namely lifetime (in *s*) has been evaluated as:

$$\tau = TP \cdot dt$$

where:

- TP is the number of time points the microtubule lives;
- dt is the sampling period (*s*).

4.6 Graphical user interface

The software was designed to be used by a staff unfamiliar with Matlab environment. Therefore, a graphical user interface (GUI) was built up in order to make the algorithm user-friendly.

In the shell (Fig. 4.4), it is asked to the user to insert the two parameter that can vary among different experiments, namely the pixel resolution and the sampling period.

Moreover, the software is suited to work in batch mode and stores results properly organized in an *excel* file, in order to ease interpretation and subsequent analysis.

TrackMTs

Pixel resolution (nm): 64

Time resolution (s): 0.5

Figure 4.4: Screenshot of the graphical interface.

Chapter 5

Results

The developed software aims to automatically analyze microtubule dynamic in fluorescence images. All information on cell behavior is extracted through some features: velocity, track length, lifetime and number of tracks detected. In detail, the first three parameters are expressed in terms of median, average and standard deviation; while regarding the number of tracks, only the mean value is displayed. All values are listed in tables properly organized to highlight the different drug effects. Indeed, even if at high concentrations the effects of both drugs are well-known, since they inhibits MTs growth, it is interesting to evaluate what happens to cells when intermediate doses are taken into account. Since the agents can be used in cancer treatment, understanding the effects at different concentrations can lead to more effective therapies.

Moreover, given the lack of a *ground truth*, in order to assess the algorithm performance, the obtained results are compared with those computed by another approach, tested on the same dataset of this work (details in [17]), and those evaluated by hand by a researcher of Department of Molecular Biotechnology and Health Sciences of Turin.

Finally, the same results are compared with other works available in literature.

5.1 General remarks

The parameter obtained through calibration, allows one to recognize about a hundred tracks in control stacks. This number is a tradeoff between selectiveness and computational time, and it was chosen as an optimal value after a debate with biologists. Indeed, if threshold is decreased (see paragraph 4.1 for further details), more tracks are recognized; therefore, false positive rate is likely to increase. Nevertheless, these trajectories are discarded downstream of the algorithm anyway, because they do not meet the rectilinear motion model.

In view of the above, as for the number of identified trajectories in the movies where cells have been doped, since both nocodazole and taxol inhibit MTs growth, one can suppose that the number of tracks should decrease by increasing drug concentration. In Tables 5.1 and 5.2, it can be seen that this hypothesis is generally confirmed, except in a few isolated cases. This is the reason why the proposed approach has proven to be conservative.

Another aspect to notice is that mean and median values exhibit little difference. It means that outliers have not a significant impact on the algorithm performance.

The last consideration is related to standard deviation values. From Tables 5.1 and 5.2, it can be seen that standard deviation levels are significant. This depends on the complexity of the problem, from both a biological and technical standpoint. This scenario is well-known to biologists and is also reported in literature.

In the next sections the detailed results are presented and discussed for both nocodazole and taxol doped cells.

5.2 Nocodazole results

Nocodazole is a “MTs destabilizer”, meaning that this drug promotes microtubule disassembly, and decreases their mass [3]. In Table 5.1 the whole results are listed for all the four increasing concentrations of nocodazole.

NOCODAZOLE

Dose	Series	v_{md}	$\bar{v}$	σ_v	λ_{md}	$\bar{\lambda}$	σ_λ	τ_{md}	$\bar{\tau}$	σ_τ	#MTs
0 nM	003	10.78	12.24	6.18	1.09	1.25	0.70	5.00	5.71	2.59	139
	005	14.95	15.36	7.75	0.87	1.02	0.69	3.50	4.33	2.00	113
	011	14.00	15.84	8.91	0.95	1.03	0.57	3.50	4.03	1.14	94
	013	14.95	14.98	6.80	1.14	1.33	0.74	4.00	5.09	2.62	200
	015	15.14	16.58	9.77	1.53	1.87	1.11	4.50	5.43	2.76	258
	Mean	**13.96**	**15.00**	**7.88**	**1.11**	**1.30**	**0.76**	**4.10**	**4.91**	**2.22**	**160**
1 nM	002	13.34	13.34	0.35	1.17	1.17	0.05	5.25	5.25	0.35	2
	005	12.83	14.00	8.04	1.05	1.25	0.59	4.00	4.57	2.01	134
	007	16.14	16.92	9.12	1.17	1.21	0.55	3.50	3.96	1.88	85
	012	16.37	17.26	8.74	0.94	1.01	0.42	3.50	4.03	1.65	48
	015	9.92	11.97	8.73	0.53	0.65	0.46	3.75	3.75	0.82	6
	Mean	**13.72**	**14.70**	**6.99**	**0.97**	**1.06**	**0.41**	**4.00**	**4.31**	**1.34**	**55**
10 nM	003	18.39	18.65	8.18	1.23	1.47	0.79	4.00	4.76	2.09	190
	005	0	0	0	0	0	0	0	0	0	0
	008	17.65	17.87	7.30	0.93	0.96	0.39	4.00	4.22	0.91	44
	011	0	0	0	0	0	0	0	0	0	0
	014	16.43	15.59	7.52	1.20	1.10	0.68	3.50	3.88	1.09	16
	Mean	**17.49**	**17.37**	**7.67**	**1.12**	**1.17**	**0.62**	**3.83**	**4.28**	**1.36**	**83**
100 nM	002	0	0	0	0	0	0	0	0	0	0
	004	0	0	0	0	0	0	0	0	0	0
	006	0	0	0	0	0	0	0	0	0	0
	009	0	0	0	0	0	0	0	0	0	0
	011	12.14	12.82	7.46	0.98	1.07	0.57	4.50	4.61	1.54	137
	Mean	**12.14**	**12.82**	**7.46**	**0.98**	**1.07**	**0.57**	**4.50**	**4.61**	**1.54**	**137**

Table 5.1: Nocodazole results. v is the velocity (µm/min); λ is the track length (µm); τ is the track lifetime (s); *#MTs* is the number of tracks detected. The subscript *md* denotes median values.

In the table, zero rows mean that the stacks have not been evaluated. This occurs if at least one of the following conditions is fulfilled:

- Noise levels are excessively high;
- No track can be identified because of drug effects.

From Table 5.1 it is clear that, increasing drug concentration, fewer stacks are evaluated; in fact, in nocodazole at 100 nM, information can be extracted only from single movie.

Mean velocity trend is displayed in Fig. 5.1 (through boxplot, in order to have a more effective view).

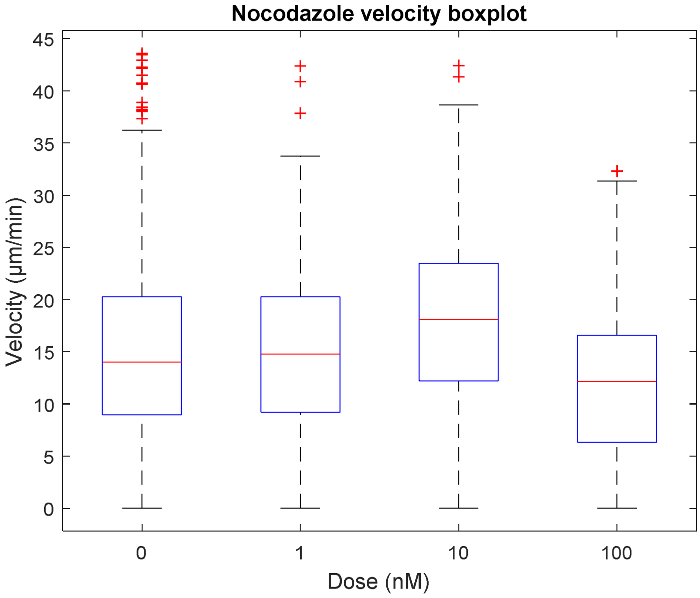

Figure 5.1: Velocity boxplot.

It can be seen that speed remains basically constant until 1 nM concentration. At 10 nM concentration a peak is shown, and then the parameter decreases at 100 nM, reaching a value lower than the starting one. Moreover, comparing global median and mean values, it is clear that they are basically the same. The only exception can be found in control stack, but this difference is due to a single sample (*series 003*).

Instead, mean length already decrease at 1 nM, and does not significantly change thereafter. It is worth pointing out that all tracks, on average, are longer than 1 µm, even if in some cases shorter tracks can be observed, e.g. s*eries 015* at 1 nM. This depends on the choice to discard, before computing parameters, all particles showing Brownian motion.

As regards lifetime, it shows a trend similar to the length one; namely it starts to decrease at 1 nM, although a little increase occurs at 100 nM. However, at that dose only one stack is taken into account.

Looking at global median and mean value of both length and lifetime, it is clear that no actual difference is shown.

The number of tracks tends to decrease at high concentrations, because even if at 100 nM a hundreds tracks are detected, it is worth pointing out that in four out five cases no tracks are found.

By focusing on standard deviation values, it is clear that they are high if compared with mean values. From comparisons, length seems to be the most critical parameter, since mean and its standard deviation have the slightest difference. This aspect can be explained by examining value distributions through histograms (Fig 5.2). As an example, only control samples have been taken into account for displaying, but a similar trend can also be found for the other concentrations. Moreover, cumulative histograms are shown, in order to have a global view.

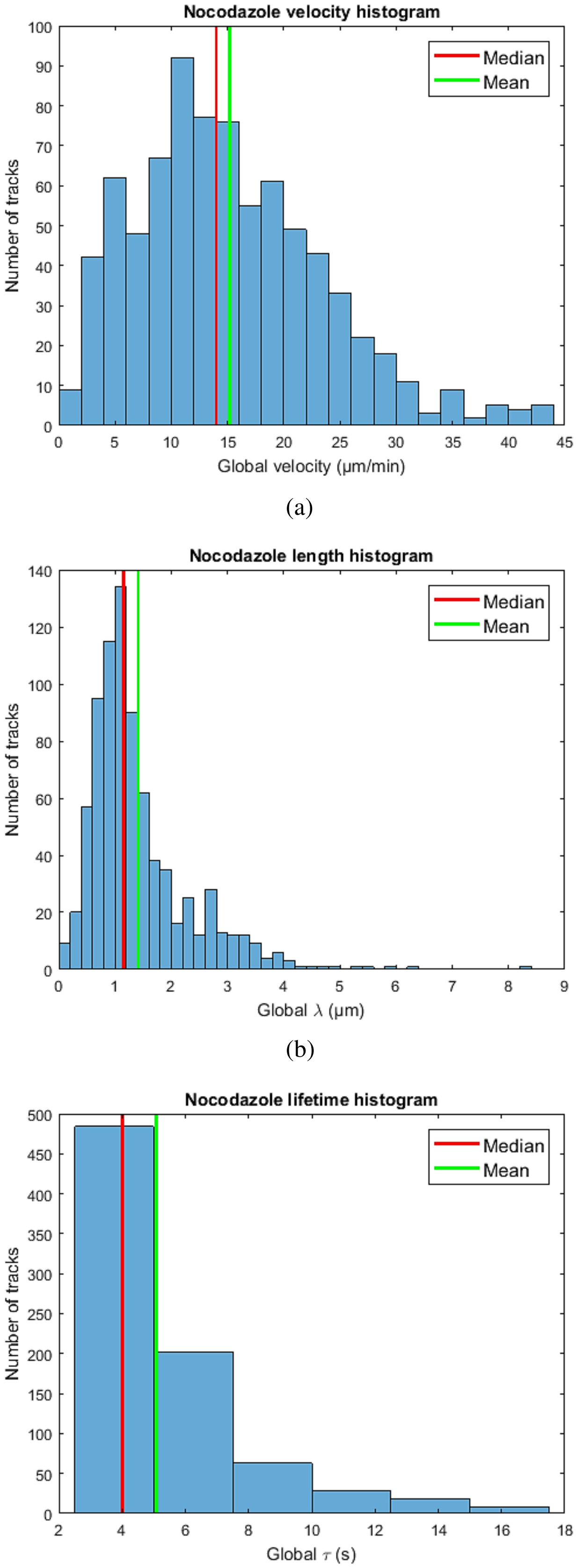

(a)

(b)

(c)

Figure 5.2: Cumulative nocodazole histograms. (a): Velocity. (b): Length. (c): Lifetime.

From Fig. 5.2a, it can be noticed that speed follows a trend that can be approximated with a truncated normal distibution, whereas Fig. 5.2b and 5.2c exhibit an exponential decay for both length and lifetime.

An important aspect to notice is that length distribution exhibits a wider variability range, if compared with velocity or lifetime; this explain why that feature can be regarded as the most critical.

5.3 Taxol results

Taxol belongs to that class of drugs called “MTs stabilizer”, so it leads to increase polymer mass, suppressing microtubule dynamics [3]. As result, fewer and shorter MTs should be detected, even if the global effects depend on the tested concentration.

In Table 5.2 all the results extracted from taxol-doped samples are listed.

TAXOL

Dose	Series	v_{md}	$\bar{v}$	σ_v	λ_{md}	$\bar{\lambda}$	σ_λ	τ_{md}	$\bar{\tau}$	σ_τ	#MTs
0 nM	Res	21.44	21.32	9.05	1.28	1.65	1.06	3.50	4.19	1.39	84
	018	23.50	22.61	10.49	1.35	1.42	0.72	3.50	4.14	1.63	69
	024	17.68	19.01	10.55	1.10	1.24	0.79	4.00	4.32	1.54	125
	028	23.25	21.14	9.07	0.87	1.11	0.71	3.00	3.77	0.96	11
	031	19.03	19.76	11.42	1.31	1.36	0.84	3.25	3.81	1.35	40
	Mean	**20.98**	**20.77**	**10.12**	**1.18**	**1.36**	**0.82**	**3.45**	**4.05**	**1.37**	**65**
0.1 nM	003	14.11	15.42	8.08	1.21	1.47	0.90	4.00	4.54	2.11	312
	006	13.11	13.55	7.30	0.92	1.16	0.66	4.00	4.60	1.83	147
	010	14.32	15.47	9.03	1.16	1.59	1.66	4.00	5.01	3.14	152
	015	14.29	15.71	8.13	1.33	1.48	0.90	4.00	4.35	1.64	283
	018	16.59	17.34	8.64	1.33	1.51	0.73	4.00	4.47	1.68	369
	025	17.26	18.00	8.87	1.14	1.46	0.88	4.00	4.80	2.08	233
	Mean	**14.95**	**15.91**	**8.34**	**1.18**	**1.44**	**0.96**	**4.00**	**4.63**	**2.08**	**249**
10 nM	006	12.14	13.26	5.67	1.06	1.33	0.70	4.50	5.52	2.56	125
	009	11.87	13.27	7.08	0.74	0.86	0.48	4.00	3.75	0.50	4
	012	11.49	12.09	5.77	1.07	1.38	0.81	4.00	5.19	2.83	106
	015	13.19	14.24	6.98	1.38	1.46	0.76	4.50	4.85	1.84	88
	018	13.84	14.43	5.36	0.59	0.68	0.31	3.00	3.67	0.97	9
	Mean	**12.51**	**13.46**	**6.17**	**0.97**	**1.14**	**0.61**	**4.00**	**4.59**	**1.74**	**66**
100 nM	002	13.10	13.61	5.78	0.82	0.92	0.55	3.50	4.27	1.41	30
	008	15.46	14.44	3.52	1.36	1.54	0.60	6.00	6.31	1.93	8
	011	21.51	21.51	0.00	1.08	1.08	0.00	3.00	3.00	0.00	1
	016	10.20	11.51	6.18	0.85	0.99	0.56	4.00	5.25	2.62	57
	019	7.68	7.68	0.00	0.49	0.38	0.00	3.00	3.00	0.00	1
	Mean	**13.59**	**13.75**	**3.10**	**0.92**	**0.98**	**0.34**	**3.90**	**4.36**	**1.19**	**19**

Table 5.2: Taxol results. v is the velocity (µm/min); λ is the track length (µm); τ is the track lifetime (s); *#MTs* is the number of tracks detected. The subscript *md* denotes median values.

The first aspect to notice is MTs behavior in control stacks. Comparing nocodazole and taxol mean values at 0 nM, it is clear that in the second scenario molecules are faster, even though cells were not doped in either case. This difference suggests the extreme variability and complexity of the problem, since cell functions are altered not only by drugs, but also by environmental factors (e.g. temperature).

In contrast to nocodazole case, the algorithm is able to extract information from all the available samples.

To discuss velocity trend, boxplot is displayed in Fig. 5.3.

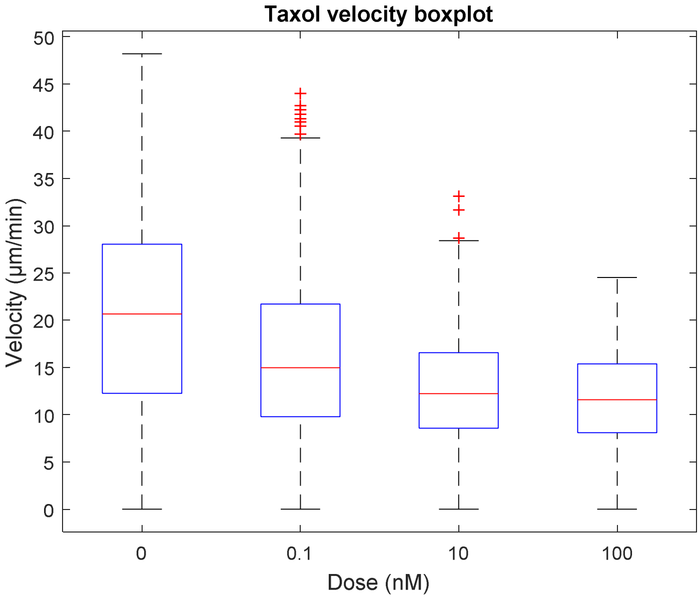

Figure 5.3: Taxol boxplot.

Speed mean values show a decreasing trend; a gap is already highlighted at very low concentration (between 0 nM and 0.1 nM). In the graph, it can be noticed that there are less outliers than in nocodazole case, and they are focused in the distribution associated with the concentration of 0.1 nM.

Moreover, analyzing single stacks behavior, s*eries 011* at 100 nM can be considered as outlier, since its value, that strongly biased global mean, is anomalous.

Moreover, mean and median speed values show irrelevant difference. Only the results at 0.1 nM are different. The gap is due to two stacks, s*eries 015* and s*eries 018*; in which an extremely high number of tracks is detected; this justifies the greater variability and the largest outlier impact.

The drug effect on the length begins to be apparent at 10 nM, when tracks become shorter, whereas at low concentrations (0 and 0.1 nM) no relevant changes occur.

Finally, lifetime increases already at 0.1 nM; this could be explained by the freezing caused by taxol, that slows down growth, without depolymerizing microtubules.

The last parameter to discuss is the number of tracks. In stacks at 0.1 nM more tracks than in control stacks are detected. This could be caused by the overall higher intensity of those movies, leading to detect false positive objects. This is the reason why the detection thresholds should be readapted, making them more selective in this specific case. However, it is worth pointing out that this high number just impacts algorithm performance from a computational standpoint, since the shortest tracks are not considered for feature evaluation, as already discussed in paragraph 5.1.

Instead, at 10 and 100 nM the trajectories detected are significantly less numerous.

Once more, standard deviations are high, and length is the most critical parameter, as in nocodazole case. Fig 5.4 shows cumulative histogram at a specific concentration of 0.1 nM. Since the same reasoning as that applied on Fig 5.2 still holds true in this case, refer to paragraph 5.2 for histogram discussion.

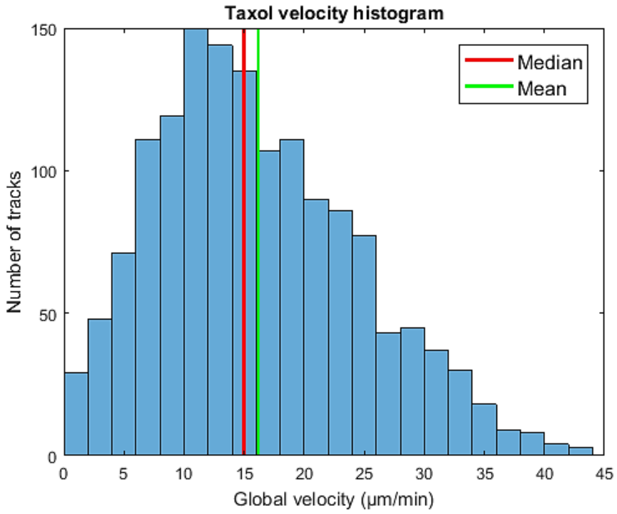

(a)

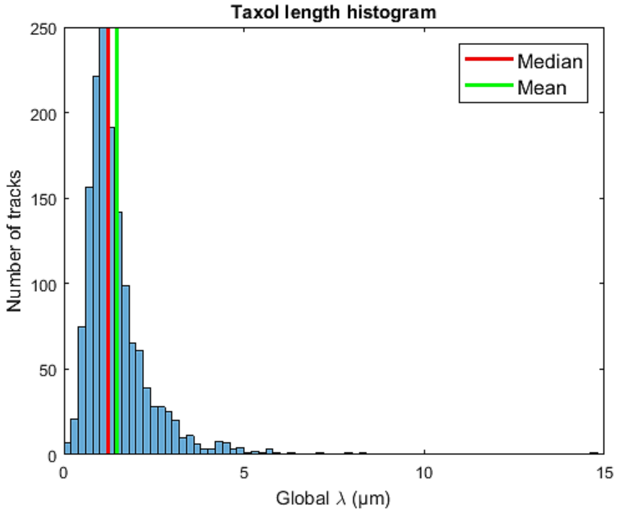

(b)

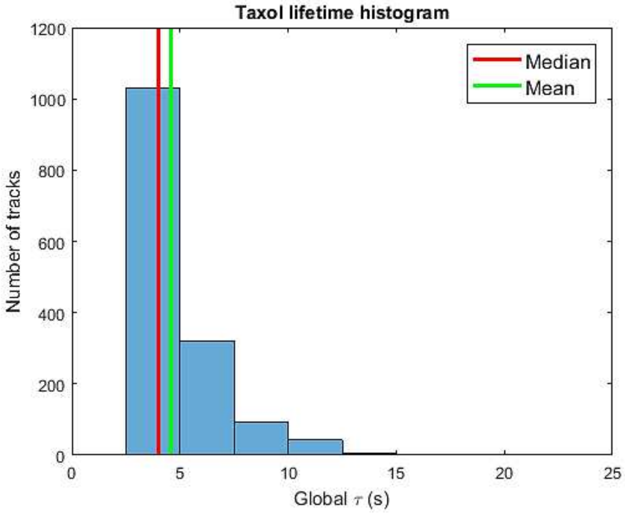

(c)

Figure 5.4: Cumulative taxol histograms. (a): Velocity. (b): Length. (c): Lifetime.

5.4 Statistical data analysis

In order to assess data reliability, in this paragraph, the standard error of the mean (*SEM*) is provided for velocity, length and lifetime.

The SEM is an indicator of the value variability among different experiments, and it is defined as:

$$SEM = \frac{\sigma}{\sqrt{N}}$$

It is clear that the standard error is related to the standard deviation of the distribution ($\sigma_v, \sigma_\lambda, \sigma_\tau$) and to the sample size (N).

In order to evaluate this parameter, for each concentration, the average standard deviation has been considered; while the sample size has been computed as the sum of the number of all tracks detected in each stack.

Table 5.3 summarizes the SEM for the three features taken into account.

NOCODAZOLE			
Dose	SEM$_v$	SEM$_\lambda$	SEM$_\tau$
0 nM	0.28	0.03	0.08
1 nM	0.42	0.03	0.08
10 nM	0.48	0.04	0.09
100 nM	0.64	0.05	0.13

TAXOL			
Dose	SEM$_v$	SEM$_\lambda$	SEM$_\tau$
0 nM	0.56	0.05	0.08
0.1 nM	0.22	0.02	0.05
10 nM	0.34	0.03	0.10
100 nM	0.31	0.03	0.12

Table 5.3: *SEM* of velocity, length and lifetime for both nocodazole and taxol.

It can be seen that, the extracted parameters, at each concentration, are characterized by non-significant differences, since the error exhibits very low values in almost all cases. Hence, it can be concluded that velocity, length and lifetime are reasonably well estimated.

5.5 Feature correlation

The three features, namely velocity, length and lifetime, were computed independently; however, it can be easily understood that their mean values are indeed correlated. To this purpose, we suppose to consider two variables as uncorrelated, then we compute the third one. Since length is the most critical parameter, as already discussed in paragraph 5.2, it is regarded as the dependent variable; while speed and lifetime are considered as the independent ones. Therefore, length is computed as:

$$\lambda = \frac{v \cdot \tau}{c}$$

In the equation v represents velocity (in *μm/min*), τ the lifetime (in *s*), and c is a conversion factor to express λ in μm.

In the following table (Table 5.4) the obtained length values are compared to the ones extracted by the algorithm.

NOCODAZOLE		
Dose	λ_{alg}	λ_{eval}
0 nM	1.30	1.23
1 nM	1.06	1.06
10 nM	1.17	1.24
100 nM	1.07	0.99

TAXOL		
Dose	λ_{alg}	λ_{eval}
0 nM	1.36	1.40
0.1 nM	1.44	1.23
10 nM	1.14	1.03
100 nM	0.98	1.00

Table 5.4: Length comparison.

It is clear that length values do not significantly differ; this proves the correlation among features and the good algorithm performance and reliability.

5.6 Algorithm performance

As previously discussed in chapter 2, there is no standard protocol to follow for microtubule tracking, because of the extreme variability of the underlying biological process. Therefore, this leads to the lack of a *ground truth* to refer to as comparison.

This is the reason why, in order to evaluate the algorithm performance, the results obtained by the approach described in this work (labeled as *Algorithm 1*), are compared with those computed by another algorithm, that we name *Algorithm 2* [17].

Moreover, the same results are compared with those computed by hand by a biologist; we name those ones *manual*.

Both mentioned comparisons are significant since all parameters refer to the same dataset used to test the approach proposed in this thesis.

Finally, the results are compared with those available in other two works. The first one is called *Algorithm 3,* and it has been proposed by *Applegate et al.* [18]; the latter is described in [16], and it is named *Algorithm 4.*

5.6.1 Comparison with *Algorithm 2*

Tables 5.5 and 5.6 summarize the comparison for both nocodazole and taxol data, through mean and standard deviation of speed, length and number of tracks identified.

The results are provided separately for the two drug types.

This comparison is discussed separately from the other two algorithms, since the same dataset of this work has been taken into account; hence, a more detailed analysis is possible.

Nocodazole results

NOCODAZOLE						
Dose	Algorithm	$\bar{v}$	σ_v	$\bar{\lambda}$	σ_λ	*#MTs*
0 nM	*Algorithm 1*	15.00	7.88	1.30	0.76	160
	Algorithm 2	16.23	13.43	1.00	1.41	393
1 nM	*Algorithm 1*	14.70	6.99	1.06	0.41	55
	Algorithm 2	*NA*	*NA*	*NA*	*NA*	*NA*
10 nM	*Algorithm 1*	17.37	7.67	1.17	0.62	83
	Algorithm 2	19.92	15.53	1.12	1.49	461
100 nM	*Algorithm 1*	12.82	7.46	1.07	0.57	137
	Algorithm 2	11.20	10.51	0.34	0.40	180

Table 5.5: Nocodazole comparison.

Table 5.5 summarizes nocodazole mean values. It is clear that average values are coherent; in fact there are not values that alter the trend of both speed and length.

As for speed values, velocity found at 10 nM with the *Algorithm 1* is lower than the one found with the second approach, but this difference can be justified by the largest number of tracks detected.

Another aspect to point out is the length difference at 100 nM. This is due to the screening process, implemented in the algorithm proposed in this work, which removes all short tracks exhibiting Brownian motion. This procedure also explains why in the second algorithm more tracks are detected than in the first one.

The last aspect to be noticed is the different velocity and length variability range in the two mentioned approaches. However, standard deviation difference is sharper for speed case than for the length one.

To better visualize trends, Fig. 5.5 plots results of both the approaches.

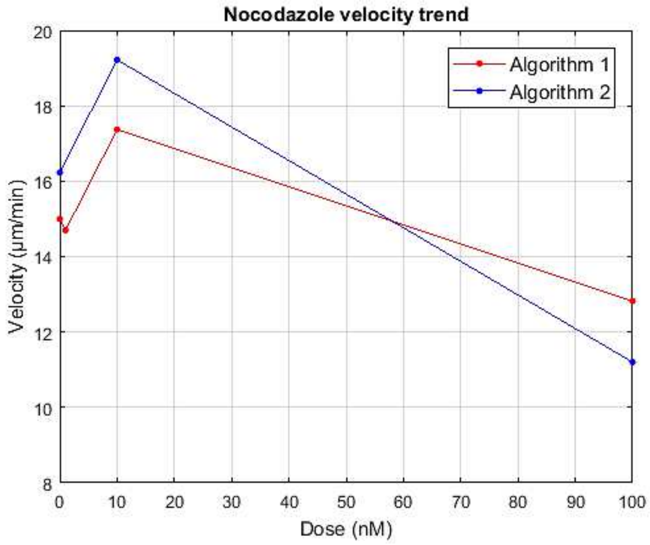

(a)

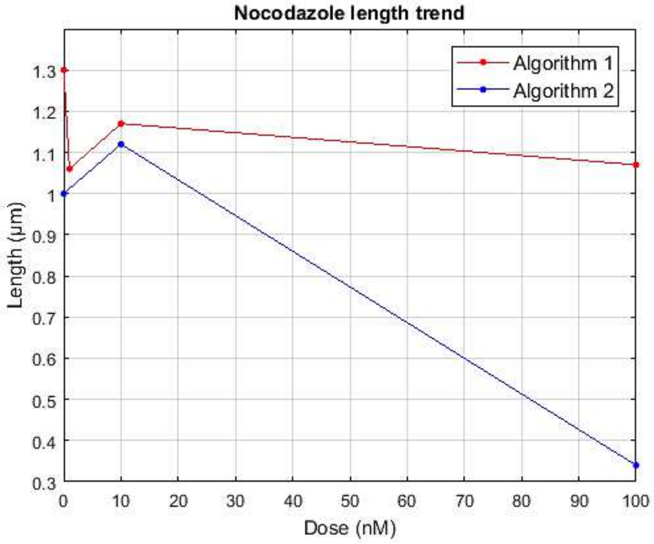

(b)

Figure 5.5: Nocodazole trend. (a): Velocity trend. (b): Length trend.

Fig. 5.5 shows that, the two algorithms yield almost the same trend for both variables. The only remarkable difference is the length value at 100 nM.

Taxol results

The following table (Table 5.6) shows all taxol comparisons.

TAXOL						
Dose	Algorithm	$\bar{v}$	σ_v	$\bar{\lambda}$	σ_λ	*#MTS*
0 nM	*Algorithm 1*	20.77	10.12	1.36	0.82	65
	Algorithm 2	22.67	17.92	1.20	1.70	428
0.1 nM	*Algorithm 1*	15.91	8.34	1.44	0.96	249
	Algorithm 2	*NA*	*NA*	*NA*	*NA*	*NA*
10 nM	*Algorithm 1*	13.46	6.17	1.14	0.61	66
	Algorithm 2	11.06	9.34	0.45	0.55	177
100 nM	*Algorithm 1*	13.75	3.10	0.98	0.34	19
	Algorithm 2	8.66	8.86	0.29	0.34	38

Table 5.6: Taxol comparison.

Table 5.6 confirms the accordance between the two approaches, already noted with nocodazole results, even if mean velocity decreases more in *Algorithm 2*. However, for both the techniques speed shows a steady decline.

Moreover, length values exhibit a difference at concentration of 10 and 100 nM; this, just like the gap between the number of tracks, can be explained again with the screening procedure.

Fig. 5.6 displays taxol speed and length results in the form of trend.

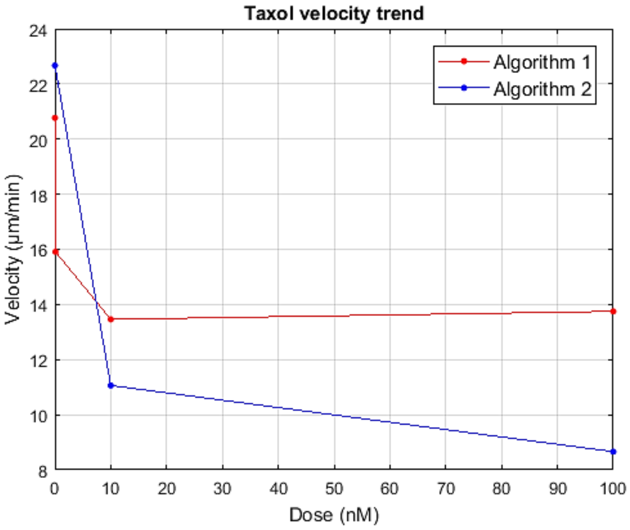

(a)

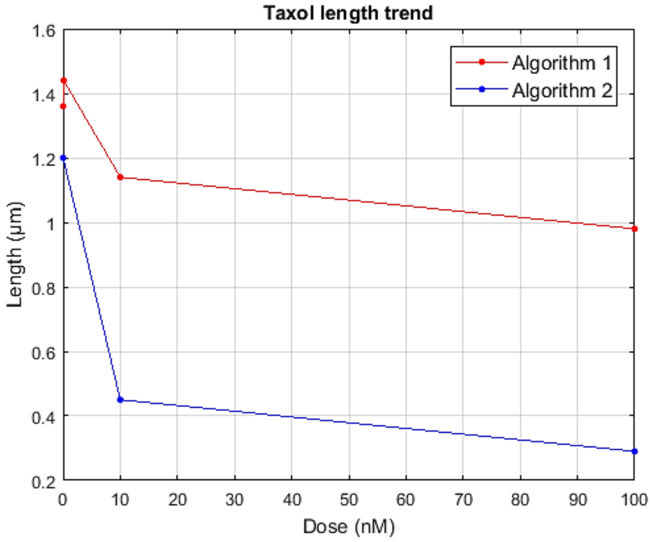

(b)

Figure 5.6: Taxol trend. (a): Velocity trend. (b): Length trend.

5.6.2 Comparison with *manual*

In this section the results of the developed algorithm are compared with those computed by hand. However, since this is a time-consuming work, not all samples have been manually evaluated. The available comparisons are listed below in Table 5.7; moreover, just mean velocity values have been taken into account.

NOCODAZOLE			
Dose	Stack ID	*Manual*	*Algorithm 1*
0 nM	003	12.03	12.24
	005	16.86	15.36
	011	16.77	15.00
1 nM	002	14.02	13.34
	005	23.53	14.00
	007	16.60	16.92

Table 5.7: Velocity comparison.

It is worth pointing out that at 1 nM tracks longer than 1 μm are taken into account. The comparison with manual work provides encouraging results. All values exhibits non-significant difference, with the exception of *series 005* of nocodazole at 1 nM concentration. However, that value can be regarded as an outlier, since it exhibit an unusual velocity value which is not found in the other cells doped with the same drug.

5.6.3 Comparison with *Algorithm 3* and *Algorithm 4*

In this last paragraph the approach proposed in this thesis is compared with other two techniques, called *Algorithm 3* [18] and *Algorithm 4* [16]. The mean results, when available, are listed below. Only speed and length values have been taken into account, and their mean and standard deviation is reported.

It is worth noticing that in [16] nocodazole and taxol-doped cells have been taken into account, but a different cell culture has been used.

Nocodazole results

NOCODAZOLE					
Dose	Algorithm	$\bar{v}$	σ_v	$\bar{\lambda}$	σ_λ
0 nM	*Algorithm 1*	15.00	7.88	1.30	0.76
	Algorithm 3	20.57	13.00	0.63	0.52
	Algorithm 4	16.00	0.75	1.45	0.30
1 nM	*Algorithm 1*	14.70	6.99	1.06	0.41
	Algorithm 3	*NA*	*NA*	*NA*	*NA*
	Algorithm 4	*NA*	*NA*	*NA*	*NA*
10 nM	*Algorithm 1*	17.37	7.67	1.17	0.62
	Algorithm 3	18.56	10.20	0.61	0.53
	Algorithm 4	*NA*	*NA*	*NA*	*NA*
100 nM	*Algorithm 1*	12.82	7.46	1.07	0.57
	Algorithm 3	17.33	11.60	0.44	0.32
	Algorithm 4	13.10*	2.25*	1.00*	0.24*

Table 5.8: Nocodazole comparison. * concentration of 80 nM.

From the previous table (Table 5.8) it can be seen that *Algorithm 3* generally shows higher mean velocity and standard deviation values than *1*; whereas, *Algorithm 1 and Algorithm 4* exhibit similar values in controls and at 100 nM. Moreover, it is worth noticing that *Algorithm 4* is characterized by a very low standard deviation, due to an algorithmic choice that suppresses variability to a large extent.

As for length, both *Algorithm 1 and Algorithm 4* yields nearly the same average values; instead, *Algorithm 3* detect much shorter tracks. This difference can be justified by the removal of the shorter tracks carried out by both *Algorithm 1 and Algorithm 4*, but not by *Algorithm 3*.

Moreover, the three algorithms show a comparable length standard deviation, without remarkable differences.

To understand the general behavior of the mentioned three algorithms, the following figure display their trend for both features.

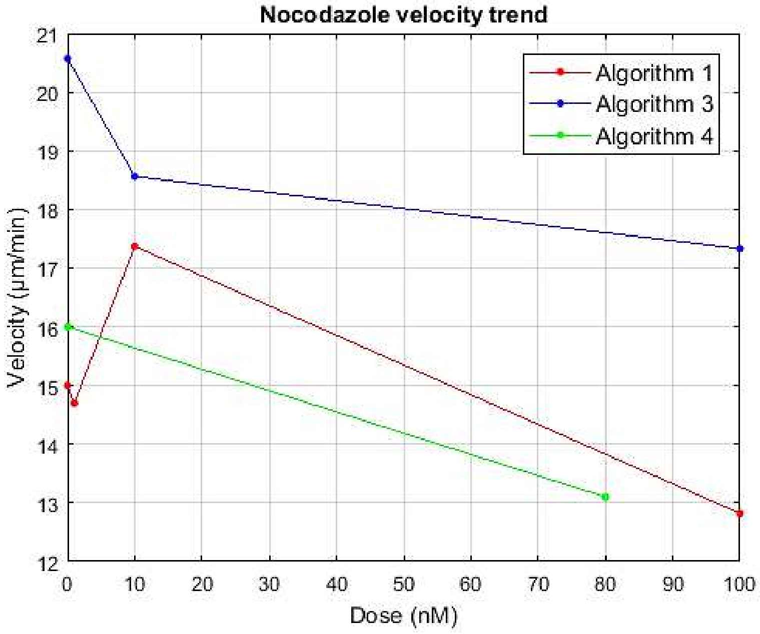

(a)

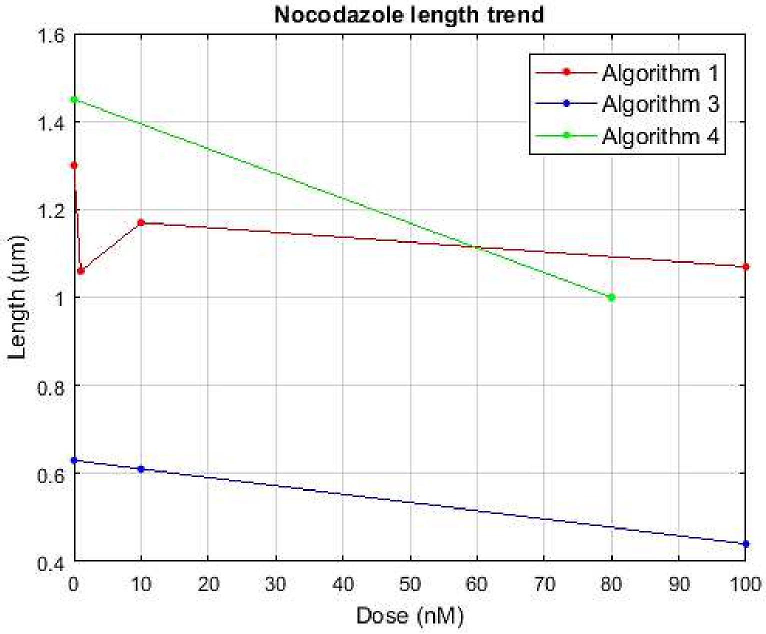

(b)

Figure 5.7: Comparison among algorithms for nocodazole. (a): Velocity trend. (b): Length trend.

In Figure 5.7 it can be observed that the compared algorithms provide results with the same order of magnitude, when the drug concentration changes.

The most interesting aspect to notice is that the *Algorithm 1*, at intermediate concentrations (i.e. 10 nM), shows an increase of MTs dynamicity in terms of velocity (see Fig. 5.7a); the same behavior was actually shown also by *Algorithm 2* (see Fig. 5.5a). Instead, velocity has a monotonic trend in the other two approaches.

This finding is significant from a biological standpoint, since it was hypothesized but rarely verified in practice, and might help to better dose nocodazole in chemotherapeutic treatments.

Taxol results

TAXOL					
Dose	Algorithm	$\bar{v}$	σ_v	$\bar{\lambda}$	σ_λ
0 nM	*Algorithm 1*	20.77	10.12	1.36	0.82
	Algorithm 3	20.44	11.10	0.67	0.58
	Algorithm 4	15.50	1.40	1.60	0.23
0.1 nM	*Algorithm 1*	15.91	8.34	1.44	0.96
	Algorithm 3	*NA*	*NA*	*NA*	*NA*
	Algorithm 4	*NA*	*NA*	*NA*	*NA*
10 nM	*Algorithm 1*	13.46	6.17	1.14	0.61
	Algorithm 3	15.25	11.60	0.40	0.32
	Algorithm 4	9.00*	1.40*	0.95*	0.15*
100 nM	*Algorithm 1*	13.75	3.10	0.98	0.34
	Algorithm 3	*NA*	*NA*	*NA*	*NA*
	Algorithm 4	7.00	1.00	0.40	0.15

Table 5.9: Taxol comparison. * concentration of 20 nM

Table 5.9 confirms the general remarks already discussed for nocodazole. However, focusing on mean velocity, *Algorithm 1* and *Algorithm 3* exhibit a similar behavior.

Finally, the three algorithms are compared through graphics (Fig. 5.8).

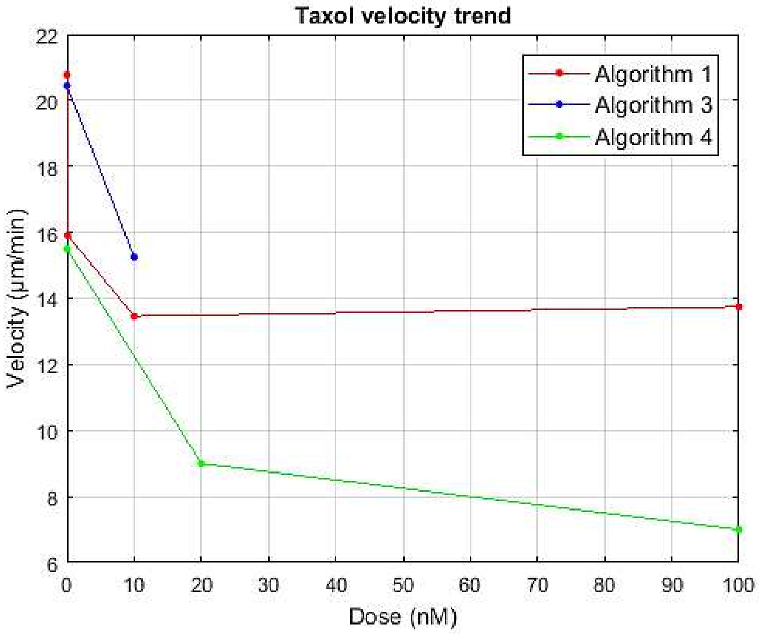

(a)

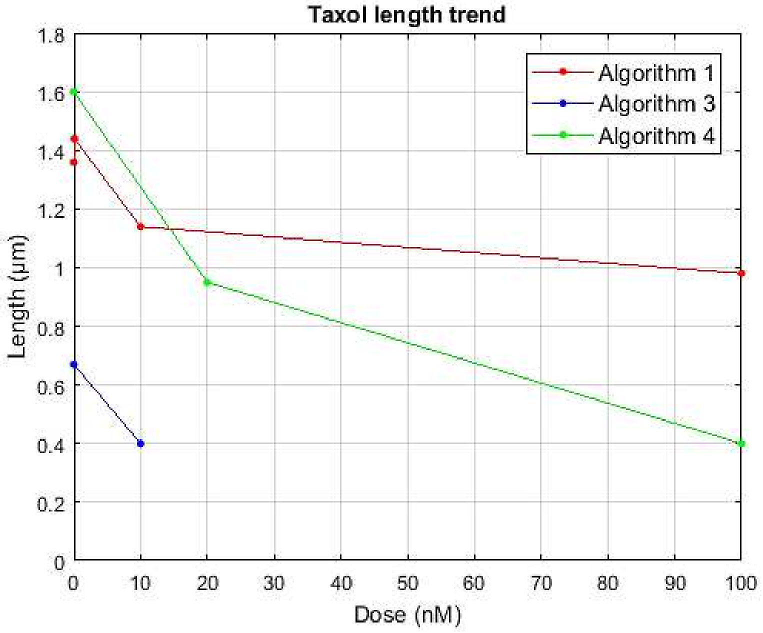

(b)

Figure 5.8: Comparison among algorithms for taxol. (a): Velocity trend. (b): Length trend.

Chapter 6

Conclusion and future directions

This work aims to supply an automatic tool for tracking and analyzing astral microtubule behavior in fluorescence images.

Despite the lack of a generally accepted *ground truth*, the validation process has provided encouraging results, which are also well-substantiated by the expected drug effects that can be found in literature.

An important matter to highlight is the benefit in terms of computational time; indeed the time spent on analyzing samples through the proposed algorithm, are considerably less, if compared to the manual labor (we are talking about several hours compared to few minutes).

Moreover, since this is an automatic software, it is not affected by human errors, due to tiredness or attention deficit, that unavoidably arise from such challenging work. Indeed, it is not uncommon that errors are committed when the analysis results are transcribed, as the gap found between manual and automatic evaluation (i.e. *series 005* of nocodazole at 1 nM) could demonstrate. This is the reason why the developed algorithm can provide a support for manual experiments, without completely replacing it.

It is worth pointing out that, with this in mind, the proposed software is currently being tested by the biologists of the Department of Molecular Biotechnology and Health Sciences of University of Turin; in this way other samples, different from those employed in this thesis, can be evaluated.

As regards future work, the algorithm might be improved with a better management of the denoising stage; moreover, in order to improve performance, detection thresholds should be adapted to each stack. Thus, problems related to the false positive rate could be further limited.

Finally, to ensure a better portability, it is planned to leave the *MathWorks* environment developing an *ImageJ* plug-in.

References

[1] C Vonesch, F Aguet, JL Vonesch, M Unser, "*The colored revolution of bioimaging*", IEEE Signal Processing Magazine, v. 23, 20–31, 2006.

[2] E Meijering, I Smal, G Danuser, "*Tracking in molecular bioimaging*", IEEE Signal Processing Magazine, 1, 46-53, 2006.

[3] SL Prosser, L Pelletier, "*Mitotic spindle assembly in animal cells: a fine balancing act*", Nat Rev Mol Cell Biol., 18(3):187-201, 2017.

[4] DA Fletcher, RD Mullins, "*Cell mechanics and the cytoskeleton*", Nature, 463(7280):485-92, 2010.

[5] Cooper GM, "*The Cell: A Molecular Approach*", 2nd edition, Sunderland (MA), Sinauer Associates, Microtubules, 2000.

[6] A Matov, K Applegate, P Kumar, C Thoma, W Krek, G Danuser and T Wittmann, "*Analysis of Microtubule Dynamic Instability Using a Plus End Growth Marker*", Nat Methods, 7(9), 761-768, 2010.

[7] E Meijering, O Dzyubachyk, I Smal, "*Methods for Cell and Particle Tracking*", Elsevier, vol. 54, 9, pp. 193-200, 2012.

[8] W J Godinez, M Lampe, S Wörz, B Müller, R Eils, and K Rohr, "*Deterministic and Probabilistic Approaches for Tracking Virus Particles in Time-lapse*

Fluorescence Microscopy Image Sequences", Med Image Anal., 13(2):325-42, 2009.

[9] P Roudot, L Ding, Member, IEEE, K Jaqaman, C Kervrann, and G Danuser, "*Piecewise-Stationary Motion Modeling and Iterative Smoothing to Track Heterogeneous Particle Motions in Dense Environments*", IEEE Transactions on Image Processing, vol 26, issue 11, pp. 5395-5410, 2017.

[10] IF Sbalzarini and P Koumoutsakos, "*Feature point tracking and trajectory analysis for video imaging in cell biology*", Journal of Structural Biology, 151 (2), 182–195, 2005.

[11] B Mahemuti, D Inoue, A Kakugo, A Konagaya, "*Investigation of the Microtubule Dynamics with Probabilistic Data Association Filter*", 11th IEEE Annual International, Japan, 2016.

[12] R Mohan, E A Katrukhaa, H Doodhi, I Smal, E Meijering, L C Kapitein, M O Steinmetzc, and A Akhmanova, "*End-binding proteins sensitize microtubules to the action of microtubule-targeting agents*", Proc. Natl Acad, 110(22), 8900–8905, 2013.

[13] B P Lucey, W A Nelson-Rees, and G M Hutchins, "*Henrietta Lacks, HeLa Cells, and Cell Culture Contamination*", Archives of Pathology & Laboratory Medicine, 133, 9, pp. 1463-1467, 2009.

[14] R Garg, A Kumar, "*Comparison of various noise removals using Bayesian framework*", International Journal of Modern Engineering Research, 2(1), pp 265-270, 2012.

[15] A Kethwas, B Jharia, "*Comparison Study on Image Denoising Though Wiener Filter*", International Journal of Engineering Research & Technology, 3(8), pp 962-966, 2014.

[16] L Sironi, J Solon, C Conrad, T U Mayer, D Brunner and J Ellenberg, "*Automatic Quantification of Microtubule Dynamics Enables RNAi-screening of New Mitotic Spindle Regulators*", Cytoskeleton, 68(5), pp. 266-278, 2011.

[17] J Levine, M Grangetto, M Varrecchia, G Olmo, "*Detection and tracking of astral microtubules in fluorescence microscopy images"*, submitted to IEEE International Conference on Image Processing 2018.

[18] K T Applegate, S Besson, A Matov, M H Bagonis, K Jaqaman, and G Danuser, "*plustiptracker: Quantitative image analysis software for the measurement of microtubule dynamics*", Journal of Structural Biology, 176(2), pp. 168-184, 2011.